



This is a repository copy of *Magnetohydrodynamic wave mode identification in circular and elliptical sunspot umbrae : evidence for high-order modes*.

White Rose Research Online URL for this paper:
<https://eprints.whiterose.ac.uk/186410/>

Version: Published Version

Article:

Albidah, A.B. orcid.org/0000-0001-7314-1347, Fedun, V. orcid.org/0000-0002-0893-7346, Aldhafeeri, A.A. et al. (7 more authors) (2022) Magnetohydrodynamic wave mode identification in circular and elliptical sunspot umbrae : evidence for high-order modes. The Astrophysical Journal, 927 (2). 201. ISSN 0004-637X

<https://doi.org/10.3847/1538-4357/ac51d9>

Reuse

This article is distributed under the terms of the Creative Commons Attribution (CC BY) licence. This licence allows you to distribute, remix, tweak, and build upon the work, even commercially, as long as you credit the authors for the original work. More information and the full terms of the licence here:
<https://creativecommons.org/licenses/>

Takedown

If you consider content in White Rose Research Online to be in breach of UK law, please notify us by emailing eprints@whiterose.ac.uk including the URL of the record and the reason for the withdrawal request.



eprints@whiterose.ac.uk
<https://eprints.whiterose.ac.uk/>



Magnetohydrodynamic Wave Mode Identification in Circular and Elliptical Sunspot Umbrae: Evidence for High-order Modes

A. B. Albidah^{1,2} , V. Fedun³ , A. A. Aldhafeeri⁴ , I. Ballai¹ , W. Brevis⁵ , D. B. Jess^{6,7} , J. Higham⁸ , M. Stangalini⁹ ,
S. S. A. Silva³ , and G. Verth¹

¹ Plasma Dynamics Group, School of Mathematics and Statistics, The University of Sheffield, Hicks Building, Hounsfield Road, Sheffield, S3 7RH, UK
abalbidah1@sheffield.ac.uk, a.albedah@mu.edu.sa

² Department of Mathematics, College of Science Al-Zulfi, Majmaah University, Al-Majmaah, 11952, Saudi Arabia

³ Plasma Dynamics Group, Department of Automatic Control and Systems Engineering, The University of Sheffield, Mappin Street, Sheffield, S1 3JD, UK

⁴ Mathematics and Statistic Department, Faculty of Science, King Faisal University, Al-Hassa, P.O. Box 400, Hofuf 31982, Saudi Arabia

⁵ School of Engineering, Pontificia Universidad Católica de Chile, Chile

⁶ Astrophysics Research Centre, School of Mathematics and Physics, Queen's University, Belfast, BT7 1NN, UK

⁷ Department of Physics and Astronomy, California State University Northridge, Northridge, CA 91330, USA

⁸ School of Environmental Sciences, Department of Geography and Planning, University of Liverpool, Roxby Building, Liverpool, L69 7ZT, UK

⁹ ASI, Italian Space Agency, Via del Politecnico snc, 00133 Rome, Italy

Received 2021 September 24; revised 2022 January 21; accepted 2022 January 31; published 2022 March 17

Abstract

In this paper, we provide clear direct evidence of multiple concurrent higher-order magnetohydrodynamic (MHD) modes in circular and elliptical sunspots by applying both proper orthogonal decomposition (POD) and dynamic mode decomposition (DMD) techniques on solar observational data. These techniques are well documented and validated in the areas of fluid mechanics, hydraulics, and granular flows but are relatively new to the field of solar physics. While POD identifies modes based on orthogonality in space and provides a clear ranking of modes in terms of their contribution to the variance of the signal, DMD resolves modes that are orthogonal in time. The clear presence of the fundamental slow sausage and kink body modes, as well as higher-order slow sausage and kink body modes, have been identified using POD and DMD analysis of the chromospheric $H\alpha$ line at 6562.808 Å for both the circular and elliptical sunspots. Additionally, for the various slow body modes, evidence for the presence of the fast surface kink mode was found in the circular sunspot. All of the MHD mode patterns were cross-correlated with their theoretically predicted counterparts, and we demonstrated that ellipticity cannot be neglected when interpreting MHD wave modes. The higher-order MHD wave modes are even more sensitive to irregularities in umbral cross-sectional shapes; hence, this must be taken into account for more accurate modeling of the modes in sunspots and pores.

Unified Astronomy Thesaurus concepts: Sunspots (1653); Solar physics (1476); Wavelet analysis (1918); Umbra (1744)

Supporting material: animations

1. Introduction

The qualitative and quantitative description of plasma dynamics in the solar and space environment is one of the most challenging aspects of solar physics. The variety of plasma motions subject to restoring forces (e.g., pressure gradient, gravitational, Lorentz, etc.) gives rise to magnetohydrodynamic (MHD) waves and oscillations. In the absence of these restoring forces, perturbations might evolve into laminar and turbulent flows, shocks, nonlinear patterns, etc. Waves have the unique property of carrying energy and information about the medium in which they propagate, making them an ideal tool for plasma and field diagnostics. However, their true diagnostic potential can be put to use only if high-resolution observations are available that could determine the accurate measurement of the wave properties and their true nature. Sunspots are the most prominent manifestations of the emergence of a magnetic field in the lower regions of the solar atmosphere, and they are often the footpoints of active regions (ARs) that are able to considerably influence the space weather. Although,

historically, sunspots are the most studied features in the solar atmosphere, their dynamical properties are far from being understood. Thanks to modern observational capabilities (from visible to near-infrared wavelengths), waves and oscillations in sunspots are observed from the photosphere to the corona. Over this height, the properties of waves (amplitude, frequency, etc.) can change due to the intrinsic changes in the plasma environment and magnetic field, making their classification and study rather difficult.

The presence of waves and oscillation of sunspots have been known since the pioneering work by Beckers & Tallant (1969), who evidenced oscillatory behavior in a sunspot by determining the observational parameters of umbral flashes. Shortly after, the 3 minute oscillations in Doppler velocity in the umbral region were identified by Beckers & Schultz (1972). Later on, it was shown that the most dominant oscillations in sunspots and pores have periods of 5 minutes at photospheric heights and 3 minutes at chromospheric heights, while global oscillations of sunspots, as a whole, have periods that range from hours to days (Nagashima et al. 2007; Stangalini et al. 2011; Jess et al. 2012, 2015; Khomenko & Collados 2015, to name but a few). In contrast, Stangalini et al. (2021) showed that the dominant oscillations of a magnetic pore observed with the Interferometric Bidimensional Spectropolarimeter have periods of 3 minutes in the photosphere,



Original content from this work may be used under the terms of the [Creative Commons Attribution 4.0 licence](https://creativecommons.org/licenses/by/4.0/). Any further distribution of this work must maintain attribution to the author(s) and the title of the work, journal citation and DOI.

instead of the expected 5 minute period, and this was the first time reporting the 3 minute oscillations in a pore photosphere. Using high-resolution observations from the Solar Optical Telescope on board Hinode, Nagashima et al. (2007) investigated the spatial distribution of the power spectral density of the oscillatory signal in and around an AR. The *G*-band data showed that in the umbra, the oscillatory power is suppressed in all frequency ranges. On the other hand, in Ca II H intensity maps, oscillations in the umbra, so-called umbral flashes, are clearly seen with the power peaking around 5.5 mHz (3 minutes). The Ca II H power distribution showed the enhanced elements with the spatial scale of the umbral flashes over most of the umbra, with a region with suppressed power at the center of the umbra. The relation between the 3 and 5 minute oscillation in sunspots was studied by Zhou & Liang (2017), who showed that the running waves are propagating across the umbra/penumbra as 3 minute oscillations when they are located at the umbra region and 5 minute oscillations in the penumbra region.

Magnetic structures observed in the solar atmosphere are perfect environments for the propagation of guided waves. Traditionally (considering only the pressure gradient and Lorentz force as restoring forces), MHD waves propagating in plasmas are classified according to their relative propagation speed (slow and fast magnetoacoustic modes, Alfvén or intermediate modes), radial structure (surface or body), and number of nodes in the radial direction (fundamental or overtone). Within the high plasma- β region, i.e., where sound speed, c_S , is greater than Alfvén speed, v_A , slow modes are propagating within the tube, mainly along magnetic field lines with the local Alfvén speed. The fast modes are allowed to propagate in any direction. Along the direction of the field lines, the fast mode travels with the sound speed, and in the direction perpendicular to the field lines, it propagates with the phase speed $v_{ph} = \sqrt{c_S^2 + v_A^2}$. In the region where the plasma- β is low ($v_A > c_S$), the slow mode propagates approximately with the local sound speed, and the fast mode propagates with the local Alfvén speed along the magnetic field lines. The angular dependence for the phase speeds of the slow and fast modes are identical in the high plasma- β region. Slow waves are prohibited from traveling perpendicular to the magnetic field lines for both high and low plasma- β regions. Surface waves propagate in a way that their maximum amplitude is attained on the boundary of the waveguide, and they are evanescent inside and outside the magnetic flux tube. In contrast, body waves have an oscillatory pattern in the radial direction inside the waveguide, and their lowest amplitude is on the boundary of the waveguide. In the external region, body waves are also evanescent (the wave power is localized and concentrated within the waveguide). The fundamental modes have only one radial node occurring at the umbra/penumbra boundary; however, overtones have more than one radial node. The MHD waves can also be classified according to their motion with respect to the longitudinal symmetry axis of the waveguide. While sausage modes propagate without perturbing the symmetry axis, kink modes perturb the axis in a back-and-forth motion. Finally, fluting modes have a complex way of perturbing the axis. Sausage and kink modes are continuously observed in solar magnetic structures (and their literature is vast); however, higher-order modes, i.e., the fluting modes, are so far elusive, and their existence is hypothetical.

Recently, Jess et al. (2017) detected slow body kink modes propagating along the azimuthal direction in a sunspot by implementing a $k - \omega$ Fourier filter (0.45–0.90 arcsec⁻¹ and 5–6.3 mHz) on H α images acquired by the Hydrogen-Alpha

Rapid Dynamics camera (HARDcam; Jess et al. 2012). More recently, Albidah et al. (2021) applied the proper orthogonal decomposition (POD; Pearson 1901) and dynamic mode decomposition (DMD; Schmid 2010) techniques for the same set of observations as Jess et al. (2017) to identify the fundamental slow body sausage and kink modes.

Keys et al. (2018) showed the separate existence of surface and body sausage modes in pores that have an approximately elliptical cross-sectional shape. The authors took a 1D crosscut along the pores and assumed that for sausage surface modes, the magnitude of the power along the time series has its maximum at the boundary and its minimum at the center, with the opposite for the sausage body mode. However, it was recently shown (Aldhafeeri et al. 2021) that the magnitude of the surface sausage mode has its maximum amplitude at the boundary along the minor axis, while it has its minimum amplitude at the boundary along the major axis. Therefore, the assumption of Keys et al. (2018) may only work for a pore that has a circular cross-sectional shape. Our present study that involves the use of the POD/DMD techniques will address this issue and show how reliable these methods are in the identification of modes in waveguides of different cross-sectional shapes.

The POD and DMD are methods that are commonly used in fluid mechanics and granular flows (Murray & Ukeiley 2007; Berry et al. 2017; Higham et al. 2017, 2020, 2021; Higham & Brevis 2018). The POD technique allows the determination of spatially orthogonal patterns from signals, while the DMD technique allows the determination of temporally orthogonal patterns, as the DMD provides a spatial pattern of the indicated modes with a pure frequency (Tu et al. 2014). Both of these methods are separately very useful and, when combined following the method developed by Higham et al. (2018), can be used to elucidate temporally and spatially orthogonal structures from solar observations; see, e.g., Albidah et al. (2021). For completeness, we provide a brief mathematical overview of the methods in Section 3.

To a very large extent, the traditional analysis of oscillations in sunspots involves applying Fourier analysis to provide the power spectra, and that can be carried out by integration over a region of interest (ROI) or even on a pixel-by-pixel basis. The assumption of a sinusoidal basis in the spatial domain can be taken as a disadvantage of using Fourier analysis, since we are applying it in a cylindrical or even an elliptical model. In the case of a cylindrical waveguide, the basis functions in the radial direction are Bessel functions, which are orthogonal to each other by definition and give the application of POD strength as the method looks at the orthogonality in space. Furthermore, POD and DMD have a further advantage over Fourier analysis, as they cross-correlate individual pixels over the ROI in the spatial and temporal domain, respectively. Moreover, the shape of the sunspot may be affected by the surrounding background, and, due to that, the shape may lose the property of orthogonality in the spatial domain; hence, the advantage of using POD will be lost, as it will not work very well anymore. However, DMD can detect modes that are orthogonal in time. Therefore, the best approach is to use the POD and DMD techniques in combination.

The wavelet time series analysis has also been widely used to study MHD wave modes and their properties in the sunspot umbra region. O’shea et al. (2002) applied wavelet and Fourier analysis on an umbral region of an observed sunspot using different spectral lines of the umbral region that covers the

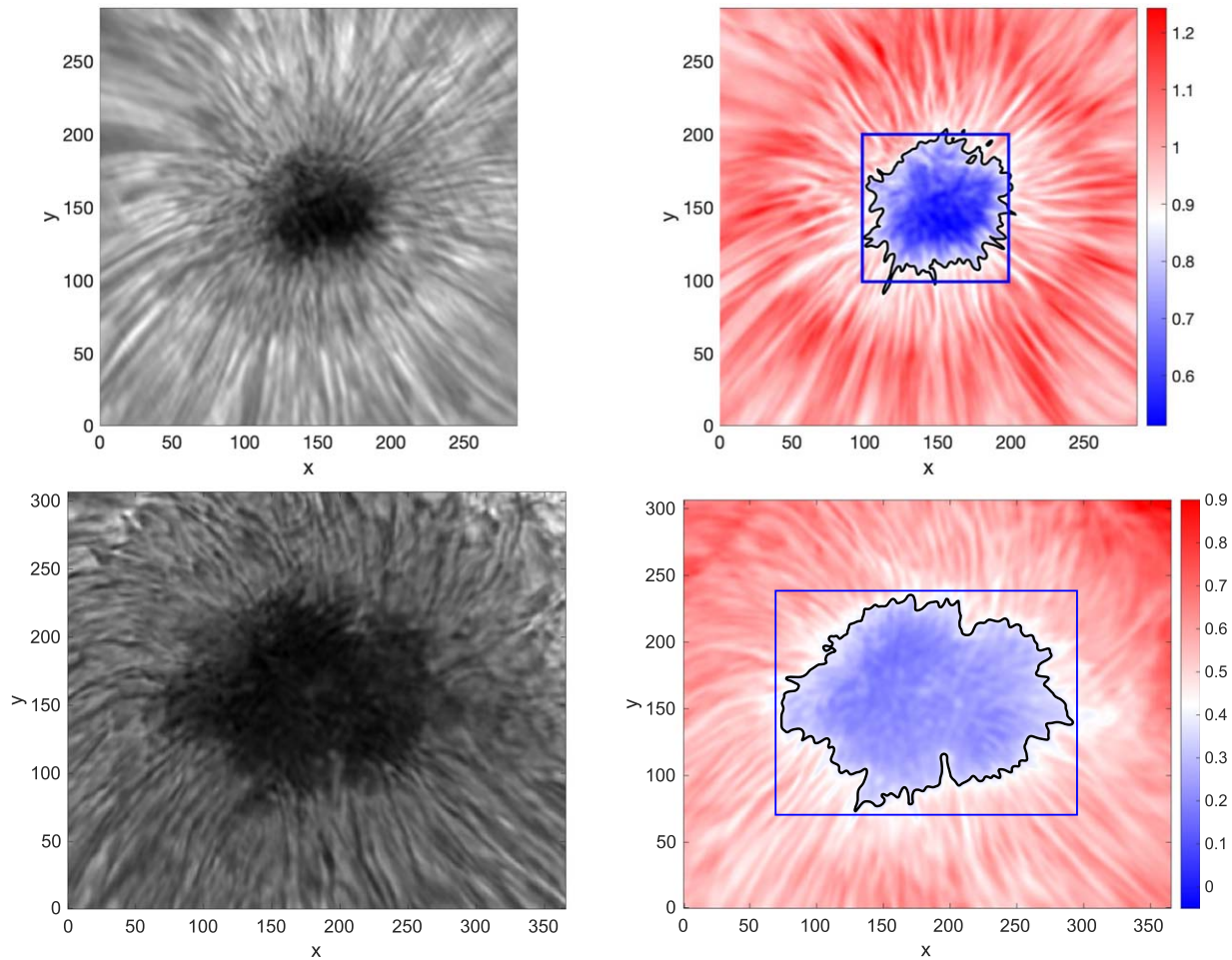


Figure 1. The first column shows snapshots from the $H\alpha$ time series of the circular (upper panel) and elliptical (lower panel) sunspot. The second column displays the mean intensity of the time series of the circular (upper panel) and elliptical (lower panel) sunspot, the color bar displays the magnitude of the mean time series, the solid black line shows the umbra/penumbra boundary with the intensity threshold level at 0.85 for the circular sunspot (and 0.4 for the elliptical sunspot), and the blue box shows the region where we apply our POD and DMD analysis.

range of temperatures from the low chromosphere to the corona to show the appearance of oscillations at all investigated temperatures, with frequencies in the range of 5.4–8.9 mHz. Christophoulou et al. (2003) used this methodology for identification of the 3 minute oscillations in the sunspot umbral region. By using radio (Nobeyama Observatory) and extreme-ultraviolet (EUV; TRACE, SDO/AIA) observations, Sych et al. (2012) applied the wavelet analysis to study the amplitude and frequency modulation of 3 minute oscillations of microwave and EUV emission generated at different heights of a sunspot atmosphere.

The existence of higher-order modes has so far mostly been predicted theoretically (see, e.g., Edwin & Roberts 1983), and the very few studies of these modes used indirect methods to show their existence. Using the observations obtained with the help of the Fast Imaging Solar Spectrograph installed at the 1.6 m Goode Solar Telescope (Kang et al. 2019) suggested that the observed two-armed spiral wave patterns in pores could be explained in terms of a superposition of slow sausage body mode (corresponding to an azimuthal wavenumber $n = 0$) and a fluting mode ($n = 2$). However, a correlation analysis between the numerically simulated and observed modes to validate the obtained results was not included in their study.

Our paper is organized as follows. A brief overview of the observations of the sunspots we study is given in Section 2.

Section 3 contains a short but necessary description of the POD and DMD techniques. The theoretical models that have been used in our analysis (the cylindrical, elliptical, and irregular shape models) are presented in Section 4. The modes' identification methodology in the circular and elliptical sunspots and the discussion of the nature of the modes are presented in Section 5. Finally, our conclusions are presented in Section 6.

2. Observations

The sunspot observations employed in the present study were both acquired using the HARDcam, which is an upgrade to the Rapid Oscillations in the Solar Atmosphere (Jess et al. 2010) imaging system available as a common-user instrument at the National Solar Observatory's Dunn Solar Telescope (DST). Each observational image sequence was acquired through a narrowband 0.25 Å (FWHM) filter centered on the chromospheric $H\alpha$ absorption line at 6562.808 Å. During each of the observing sequences, high-order adaptive optics (Rimmele 2004) were employed, with the acquired images further improved through the application of speckle reconstruction algorithms (Wöger et al. 2008). Specific acquisition details are provided below.

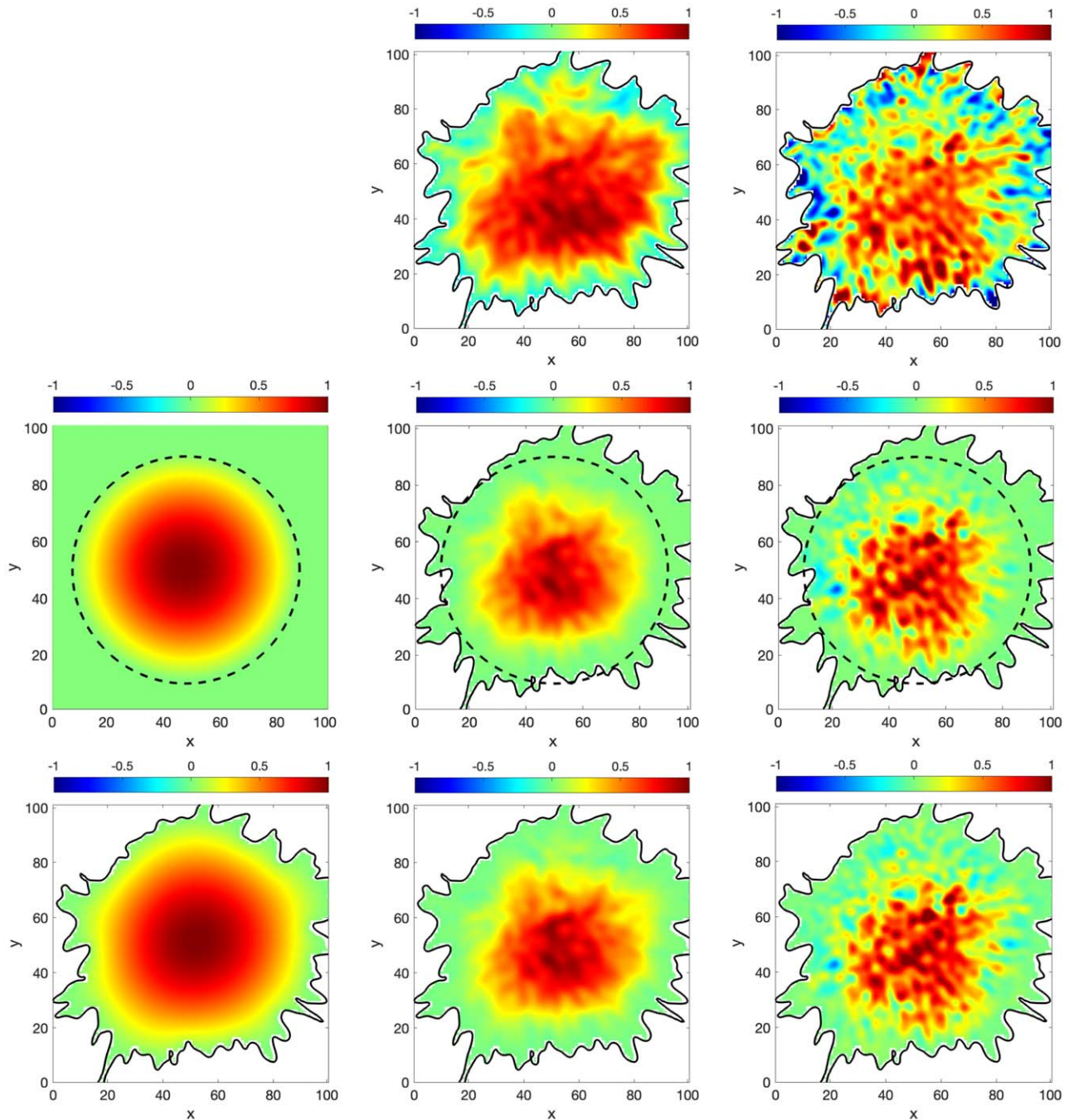


Figure 2. The first row displays the spatial structure of the modes that were detected from the observational data: the first POD mode (middle) and the DMD mode that corresponds to the frequency of 4.8 mHz (right) (Albidah et al. 2021). In the first column, we display the theoretical spatial structure of the fundamental slow body sausage mode in the cylindrical magnetic flux tube model (middle) and the corresponding structure considering the realistic sunspot with irregular shape (bottom). The rest of the panels show the cross-correlation between theoretically constructed and observationally detected modes, and the positive/negative numbers in the color bar denote correlation/anticorrelation. The dashed circles show the boundary of the tube, and the solid black line shows the umbra/penumbra boundary. The 3D visualization of this mode can be found in Figure 21 in the Appendix. The same configuration was used for Figures 3–6.

2.1 2011 December 10

The sunspot formed part of NOAA 11366, which was located at heliocentric coordinates ($356''$, $305''$), or N18W22 in the conventional heliographic coordinate system. A pixel size of $0.''138 \text{ pixel}^{-1}$ was chosen to provide a field-of-view size equal to $71'' \times 71''$. Images were acquired over the course of 75 minutes (16:10–17:25 UT) at a cadence of 0.050 s. The data set had previously been employed in a host of scientific studies (Jess et al. 2013, 2016, 2017; Krishna Prasad et al. 2015;

Albidah et al. 2021) due to the excellent seeing conditions and the highly circularly symmetric shape of the sunspot umbra. Following speckle techniques, the final cadence for the reconstructed images is 1.78 s. A sample $H\alpha$ image of the sunspot is displayed in the upper left panel of Figure 1.

2.2 2014 August 24

The sunspot formed part of NOAA 12146, which was located at heliocentric coordinates ($496''$, $66''$), or N10W32 in

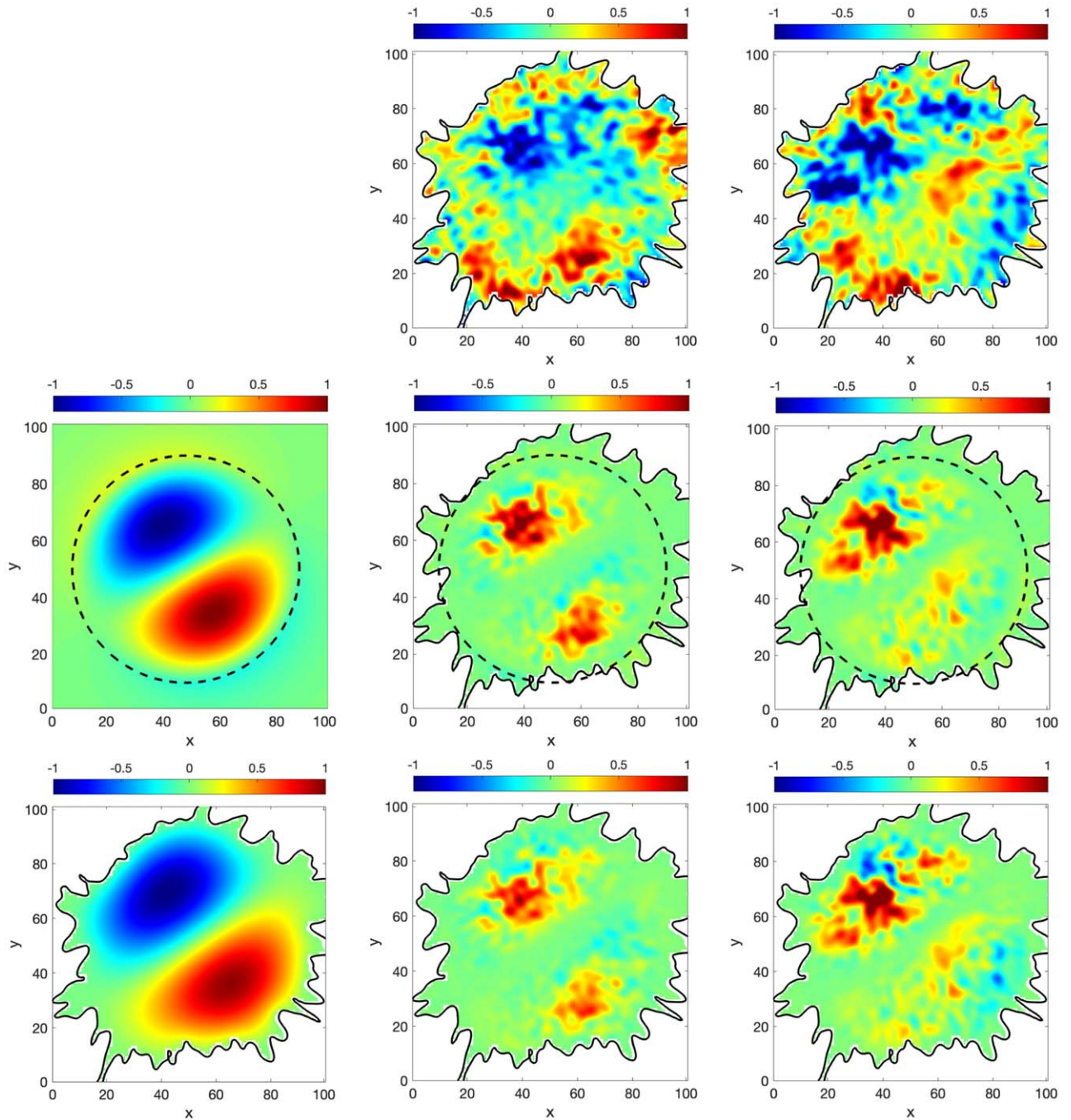


Figure 3. The 13th POD (top row, first panel) and DMD mode (top row, second panel) with a frequency of 6 mHz, which has an azimuthal symmetry of the fundamental slow body kink mode (Albidah et al. 2021). The 3D visualization of this mode is shown in Figure 21 in the Appendix.

the conventional heliographic coordinate system. A diffraction-limited pixel size of $0''.108 \text{ pixel}^{-1}$ was chosen to provide a field-of-view size equal to $180'' \times 180''$, which is the maximum allowable by the DST optics. Images were acquired over the course of 120 minutes (13:56–15:56 UT) at a cadence of 0.017 s. The data set had previously been employed in a study that examined the presence of Alfvén-wave-driven shocks in sunspot atmospheres (Grant et al. 2018). Following speckle techniques, the final cadence for the reconstructed images is 1.00 s. A sample $H\alpha$ image of the sunspot is displayed in the lower left panel of Figure 1.

3. POD and DMD Analysis of Observational Data

For both the POD and DMD, we consider a sequence of ROI intensity snapshots of a time domain of size T and a spatial domain of size $X \times Y$, with each snapshot regularly temporally spaced. Each snapshot is column vectorized such that $N = XY$, and a matrix W is created from them such that $W \in N \times T$. To apply the POD technique, we use a singular-value decomposition (SVD):

$$W = \Phi S C^* \quad (1)$$

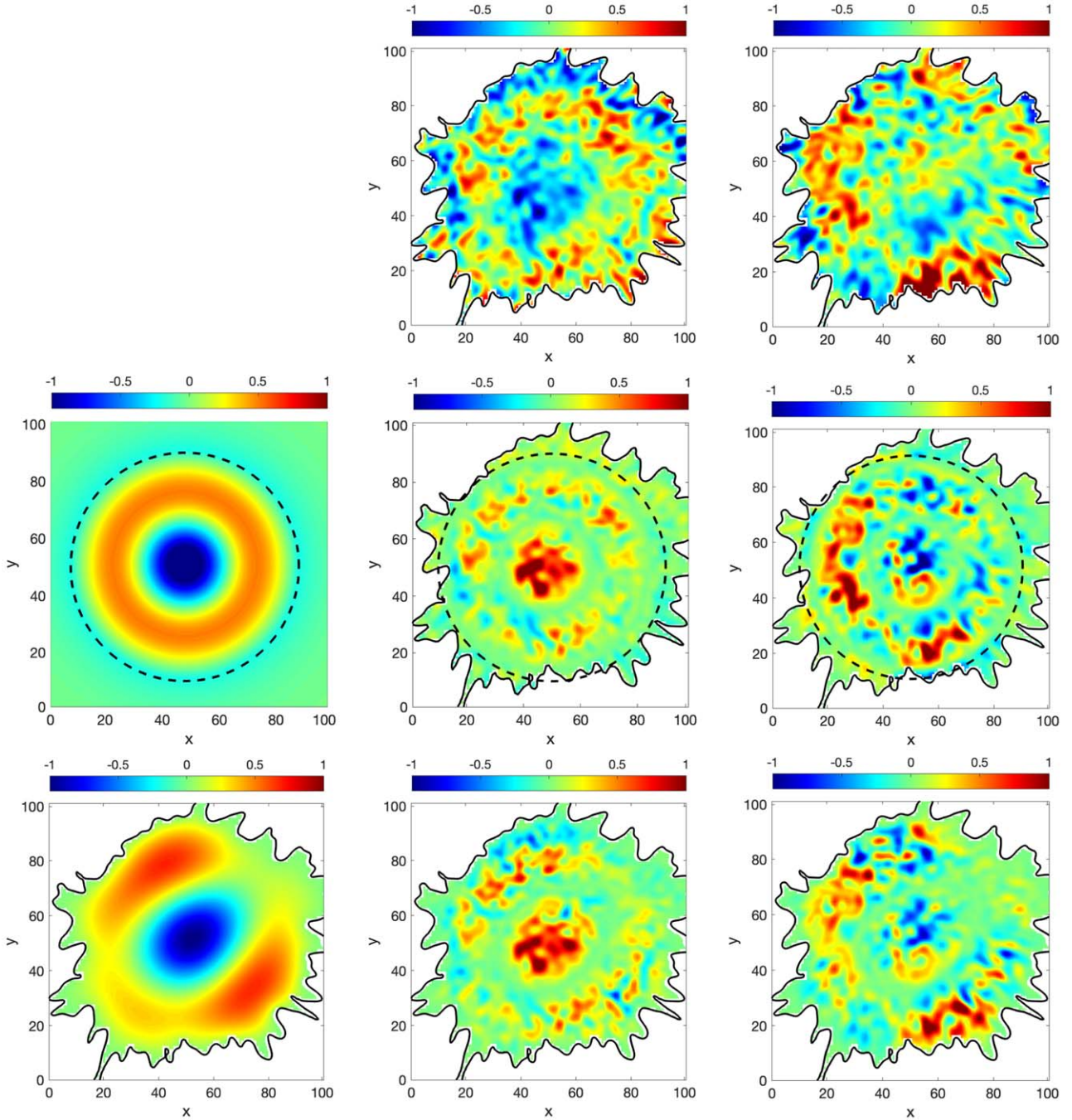


Figure 4. The 19th POD (top row, first panel) and DMD mode (top row, second panel) with a frequency of 5.6 mHz, which has an azimuthal symmetry of the slow body sausage overtone mode. The 3D visualization of this mode is shown in Figure 21 in the Appendix.

The decomposition results in the spatial structure of each mode are given in the form of columns of the matrix Φ , and their temporal evolution is given by the columns of the matrix C , where an asterisk denotes a conjugate transpose operation. Modes are ranked according to their contribution to the total variance of the snapshot series. This contribution is given by the diagonal elements of matrix λ by means of the vector $\lambda = \text{diag}(S)^2/(N)$.

To perform DMD, analogously to POD, the snapshots are organized in columns but in two matrices, W^A and W^B , such that W^B is shifted by a snapshot of W^A . Then, the matrix W^A is

decomposed using the SVD:

$$W^A = \tilde{\Phi} \tilde{S} \tilde{C}^* \quad (2)$$

Using this result and the matrix W^B , the matrix

$$F = \tilde{\Phi} W^B \tilde{C} S^{-1} \quad (3)$$

is obtained. Using the matrix F , we can calculate its complex eigenvalues, μ_i , and eigenvectors, z_i , where $i = 1 \dots \tau$ and $\tau = T - 1$. According to Schmid (2010), to create a robust set of eigenvectors, a Vandermonde expansion of the eigenvalues

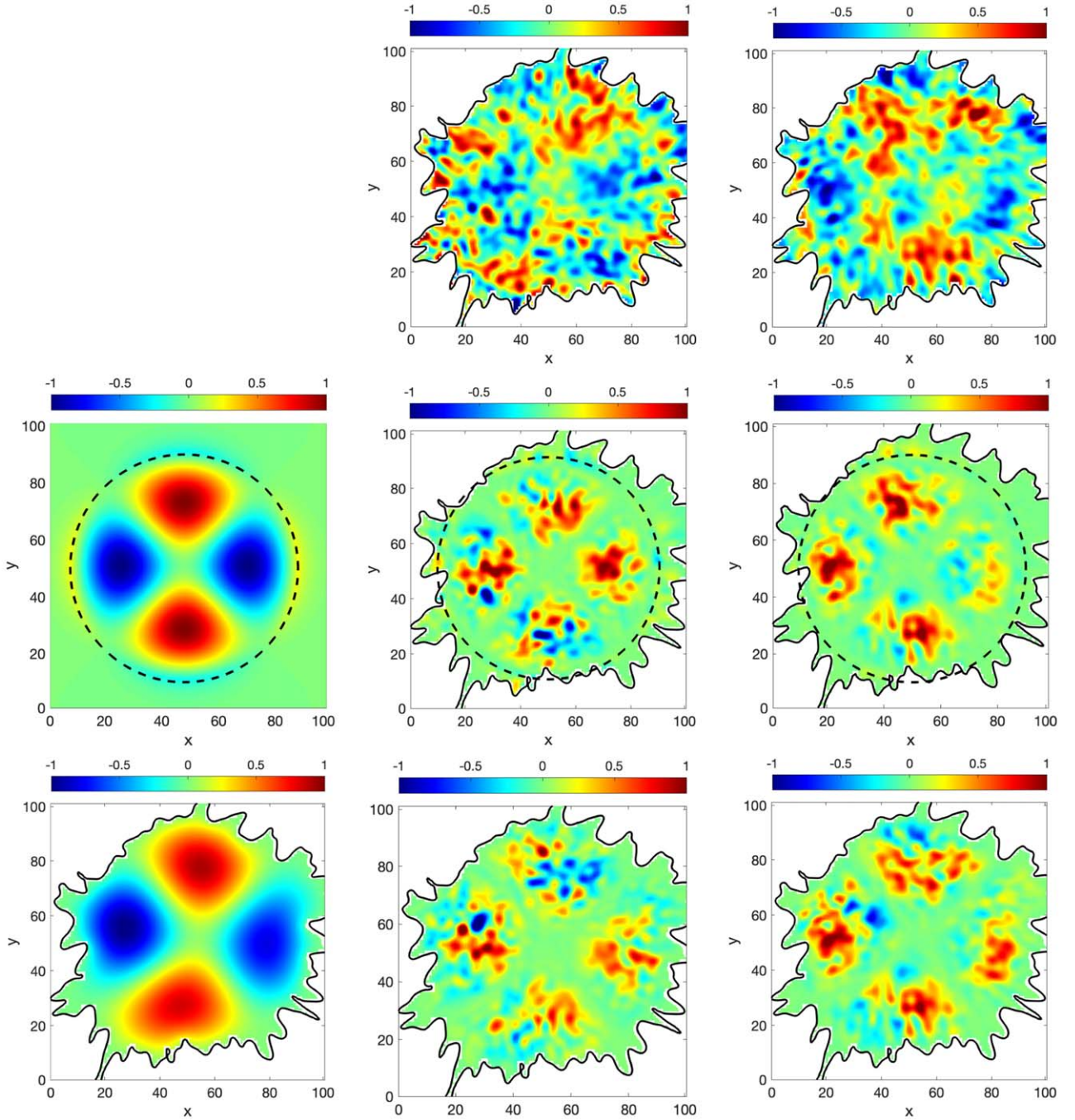


Figure 5. The 20th POD (top row, first panel) and DMD mode (top row, second panel) with a frequency of 7.6 mHz, which has an azimuthal symmetry of the slow body fluting mode ($n = 2$). The 3D visualization of this mode is shown in Figure 21 in the Appendix.

can be employed as

$$\mathcal{Q}_{i,j} = \mu_i^{j-1}, \quad (4)$$

where $i = 1 \dots \tau$ and $j = 1 \dots \tau$. The spatial modes of DMD are calculated by

$$\Psi = \mathbf{W}^A \mathbf{Q}^*, \quad (5)$$

and the frequencies associated with these modes can be determined using

$$f_i = f_s \arg(z_i) / 2\pi, \quad (6)$$

where f_s is the snapshot-sampling frequency. Following the approach by Higham et al. (2017, 2018), modes are identified based on their contribution to the variance via POD. This step is followed by the calculation of a Fourier power spectrum of the POD time coefficients associated with the dominant modes. These spatially important frequencies can then be used to identify temporally orthogonal modes determined by the DMD.

4. Models

The behavior of MHD waves in sunspots approximated by magnetic configurations, such as a cylinder with a circular or an elliptical cross section, can be understood by analyzing

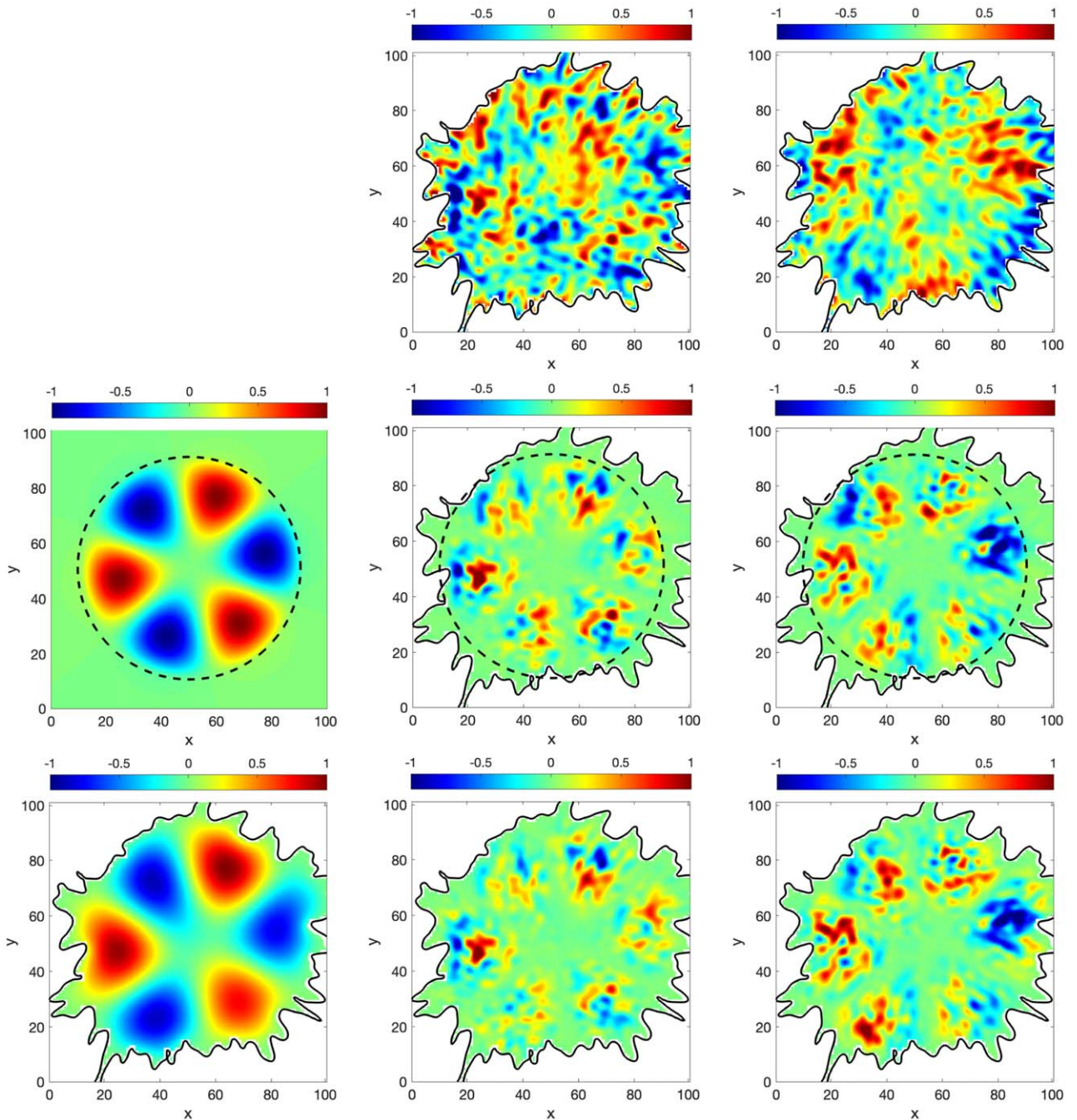


Figure 6. The 26th POD (top row, first panel) and DMD mode (top row, second panel) with a frequency of 7.4 mHz, which has an azimuthal symmetry of the slow body fluting mode ($n = 3$). The 3D visualization of this mode is shown in Figure 21 in the Appendix.

dispersion relations derived from the full set of MHD equations. More complicated cases (when the sunspot's cross-section shape is irregular) can be studied only numerically. In this study, we used all three types of models describing MHD wave propagation in magnetic flux tubes and compared the theoretically predicted waves' signature with observed data using correlation techniques.

The first model is the cylindrical model with a circular cross section, and the predictions of this model are compared with the modes that are observed from the circular sunspot (see Figures 2–6). The second model describes the possible wave modes in a waveguide with an elliptical cross section. The predictions of this model are compared with the observational data derived using the sunspot with an approximately elliptical

shape (see Figures 8–13). Finally, the third model assumes an irregular cross-sectional shape. The theoretical predictions were compared to both sunspot types, i.e., the circular (see Figures 2–6) and elliptical (see Figures 8–13).

4.1. Cylindrical Model

Following the standard approach, we assume a magnetic flux tube with a circular cross section of radius a . The axis of the tube is oriented along the vertical z -axis. We will denote the quantities that correspond to each of the internal and external regions with the indices i and e , respectively. The plasma is permeated by a homogeneous magnetic field directed along the longitudinal symmetry axis (B_i and B_e , respectively) and

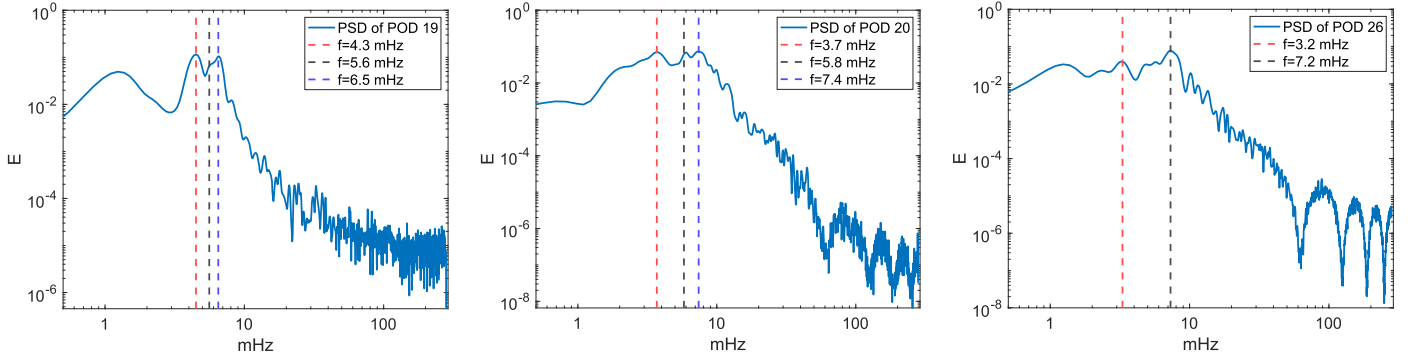


Figure 7. The PSD of the time coefficients of the POD 19 (left panel), POD 20 (middle panel), and POD 26 (right panel) modes. The vertical colored dashed lines represent the values in the frequency domain that correspond to the peaks of the PSD, and the values of the peaks' locations are shown in the legend of each figure. The PSD of POD 1 and POD 13 (the fundamental sausage and kink modes) can be found in our earlier study (Albidah et al. 2021).

Table 1
Summary of the Properties of the MHD Modes Detected by the POD and DMD Techniques in the Sunspot with a Circular Cross Section

MHD Wave Mode	m_i	f (mHz)	k_z (Mm^{-1})	λ (Mm)	V_{ph} (km s^{-1})
Fundamental slow body sausage	1.0353	4.8	3.0022	2.0928	10.04
Fundamental slow body kink	1.6765	6	3.73754	1.6811	10.08
Slow body overtone sausage	2.3754	5.6	3.395	1.8507	10.36
Slow body fluting ($n = 2$)	2.214	7.6	4.7294	1.3285	10.09
Slow body fluting ($n = 3$)	2.7471	7.4	4.55619	1.3790	10.20

Note. The first column contains the names of the modes, while the second column shows the value of the magnetoacoustic parameter, m_i (see Equation (9)). The third column contains the frequency determined from the DMD analysis. The fourth column contains the wavenumber along the vertical direction, calculated by means of Equation (9), with $\omega = 2\pi f$, $c_i = 0.01$ (Mm s^{-1}), and $v_{Ai} = 4c_i$. The fifth column shows the wavelength ($\lambda = 2\pi/k_z$), while the sixth column gives the phase speed ($V_{\text{ph}} = f\lambda$) of the identified modes.

Table 2
Summary of the MHD Wave Properties that Were Detected by the POD and DMD Techniques in the Sunspot with an Elliptical Cross Section

MHD Wave Mode	\tilde{m}_i	f (mHz)	k_z (Mm^{-1})	λ (Mm)	V_{ph} (km s^{-1})
Fundamental slow body sausage	1.1644	3.5	2.24887	2.7939	9.77
Fundamental slow body kink	1.6368	5.88	3.7696	1.6667	9.80
Slow body overtone kink	3.1698	5.3	3.412798	1.8410	9.75
Slow body fluting ($n = 2$)	2.6328	5.61	3.6166	1.7373	9.74
Slow body fluting ($n = 3$)	2.7837	6.2	3.995553	1.5725	9.74

Note. The first column contains the types of the modes, and the value of the magnetoacoustic parameter, \tilde{m}_i , is shown in the second column (see Equation (13)). The third column contains the frequency of the waves, as determined from the DMD analysis. The fourth column contains the wavenumber along the vertical direction of the sunspot, and it is calculated using Equation (13), with $\omega = 2\pi f$, $c_i = 10$ km s^{-1} , $v_{Ai} = 4c_i$, and $\sigma^2 = 0.4174$. The fifth column shows the wavelength ($\lambda = 2\pi/k_z$) of the waves, while the sixth column contains the phase speed ($V_{\text{ph}} = f\lambda$) of the waves. All units of physical quantities are shown in the table.

characterized by constant plasma densities (ρ_i and ρ_e) and kinetic pressures (p_i and p_e). Assuming a regular solution along the symmetry axis and a localized dynamics inside the flux tube (i.e., exponentially decaying solutions outside the magnetic cylinder), the dispersion relations of the surface and body modes can be given as (see Edwin & Roberts 1983, for more details)

$$\begin{aligned} & \rho_i(k_z^2 v_{Ai}^2 - \omega^2) m_e \frac{K'_n(m_e a)}{K_n(m_e a)} \\ &= \rho_e(k_z^2 v_{Ae}^2 - \omega^2) m_i \frac{I'_n(m_i a)}{I_n(m_i a)}, \end{aligned} \quad (7)$$

$$\begin{aligned} & \rho_i(k_z^2 v_{Ai}^2 - \omega^2) m_e \frac{K'_n(m_e a)}{K_n(m_e a)} \\ &= \rho_e(k_z^2 v_{Ae}^2 - \omega^2) m_i \frac{J'_n(m_i a)}{J_n(m_i a)}, \end{aligned} \quad (8)$$

where k_z is the wavenumber in the vertical direction; $v_{Ai} = B_i / \sqrt{\mu_0 \rho_i}$ and $v_{Ae} = B_e / \sqrt{\mu_0 \rho_e}$ are the Alfvén speeds inside and outside the flux tube; ω is the frequency of the waves; I_n , J_n , and K_n are the Bessel functions of order n ; μ_0 is the permeability of free space; and the dash denotes the derivative of the Bessel functions with respect to their argument. The magnetoacoustic parameters, m_i and m_e , are defined as

$$\begin{aligned} m_i^2 &= \frac{(k_z^2 c_i^2 - \omega^2)(k_z^2 v_{Ai}^2 - \omega^2)}{(c_i^2 + v_{Ai}^2)(k_z^2 c_i^2 - \omega^2)} \quad \text{and} \\ m_e^2 &= \frac{(k_z^2 c_e^2 - \omega^2)(k_z^2 v_{Ae}^2 - \omega^2)}{(c_e^2 + v_{Ae}^2)(k_z^2 c_e^2 - \omega^2)}. \end{aligned} \quad (9)$$

The signs of these parameters determine the nature of the MHD waves, e.g., Equation (7) with $m_i^2 > 0$ corresponds to the

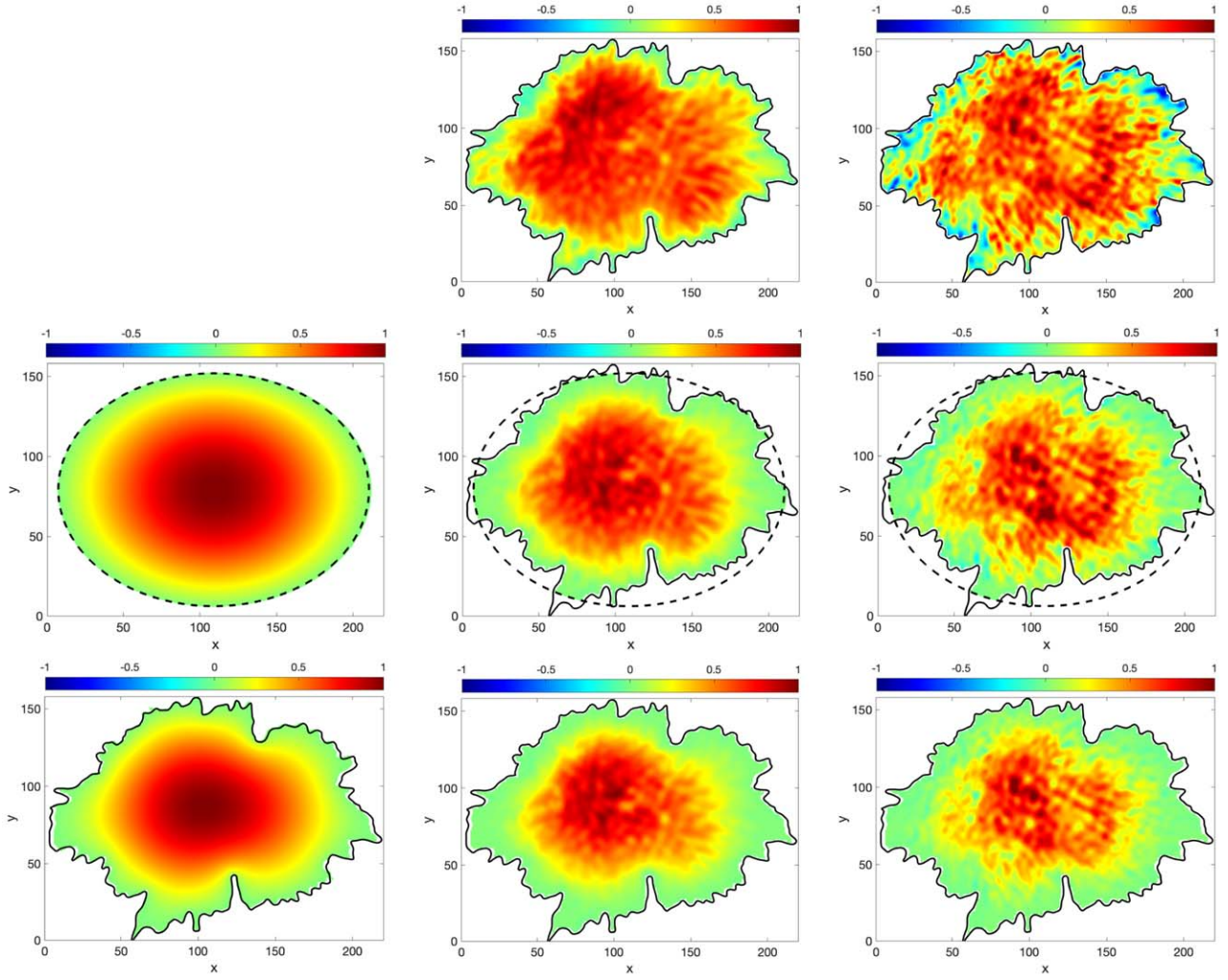


Figure 8. The first row displays the spatial structure of the first POD mode (left panel) and the DMD mode that corresponds to 3.4 mHz (right panel). The first column displays the theoretical modes of the fundamental slow body sausage mode in an elliptical magnetic flux tube (middle) and the theoretical modes of the fundamental sausage body mode in the irregular shape that corresponds to the actual sunspot shape (bottom). The rest of the panels show the cross-correlation between theoretically constructed and observationally detected modes, and the positive/negative numbers on the color bar denote correlation/anticorrelation. The dashed ellipse shows the boundary of the flux tube, and the solid black line shows the umbra/penumbra boundary. The 3D visualization of this mode is displayed in Figure 22 in the Appendix. The same configuration is used for Figures 10–13.

dispersion relation of surface waves, and Equation (8) with $m_i^2 < 0$ describes the body waves. In the case of both modes, the condition $m_e^2 < 0$ ensures an exponentially decaying solution outside the magnetic flux tube. In the above expressions, $c_{Si} = \sqrt{\gamma p_i / \rho_i}$ and $c_{Se} = \sqrt{\gamma p_e / \rho_e}$ are the adiabatic sound speeds, γ is the ratio of specific heats, and the quantities c_{Ti} and c_{Te} are the characteristic speeds of the slow magnetoacoustic mode (tube) speeds in the two regions, defined as

$$c_{Ti}^2 = \frac{v_{Ai}^2 c_i^2}{v_{Ai}^2 + c_i^2} \text{ and } c_{Te}^2 = \frac{v_{Ae}^2 c_e^2}{v_{Ae}^2 + c_e^2}. \quad (10)$$

The values of the parameter n determine the symmetry of the mode with respect to the axis of the magnetic flux tube; that is, $n = 0$ corresponds to sausage modes, $n = 1$ to kink modes, and $n \geq 2$ to fluting modes.

4.2. Elliptical Model

The model describing the wave propagation in a cylindrical magnetic flux tube (Edwin & Roberts 1983) can be expanded

to a more general case of a magnetic waveguide with an elliptical cross section (see Aldhafeeri et al. 2021, for more details). In this configuration, dispersion equations for MHD surface and body waves can be represented as

$$\begin{aligned} \rho_{0e} (k_z^2 v_{Ae}^2 - \omega^2) \frac{\Xi_m'^{E,O}(|\tilde{m}_i|, s_0)}{\Xi_m^{E,O}(|\tilde{m}_i|, s_0)} \\ = \rho_{0i} (k_z^2 v_{Ai}^2 - \omega^2) \frac{\Psi_m'^{E,O}(|\tilde{m}_e|, s_0)}{\Psi_m^{E,O}(|\tilde{m}_e|, s_0)}, \end{aligned} \quad (11)$$

$$\begin{aligned} \rho_{0e} (k_z^2 v_{Ae}^2 - \omega^2) \frac{\Theta_m'^{E,O}(\tilde{m}_i, s_0)}{\Theta_m^{E,O}(\tilde{m}_i, s_0)} \\ = \rho_{0i} (k_z^2 v_{Ai}^2 - \omega^2) \frac{\Psi_m'^{E,O}(|\tilde{m}_e|, s_0)}{\Psi_m^{E,O}(|\tilde{m}_e|, s_0)}. \end{aligned} \quad (12)$$

Here the new magnetoacoustic parameters are

$$\tilde{m}_i^2 = -\frac{\sigma^2}{4} m_i^2, \quad \tilde{m}_e^2 = -\frac{\sigma^2}{4} m_e^2, \quad (13)$$

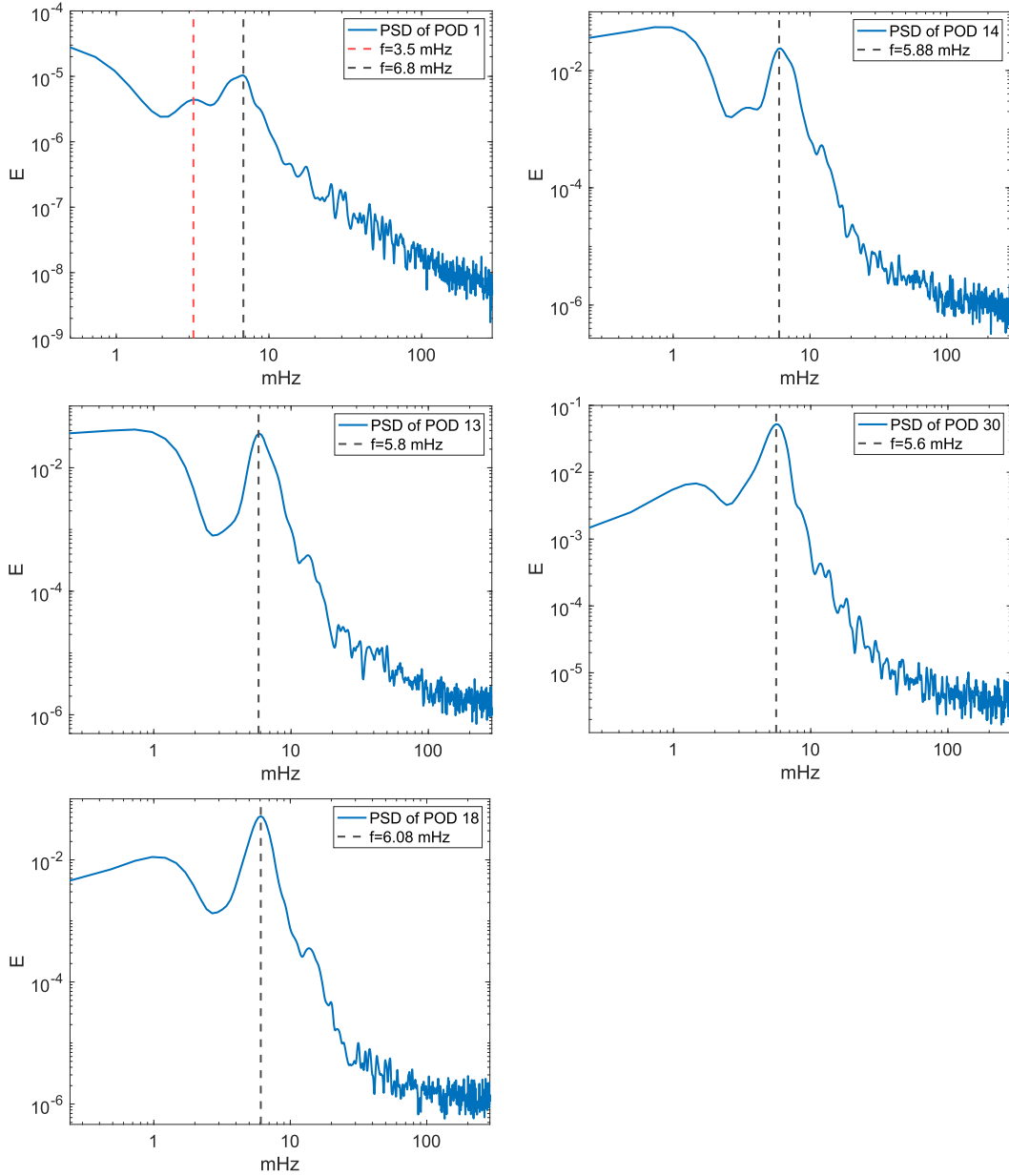


Figure 9. The PSD of the time coefficients of the POD 1 (top left panel), POD 14 (top right panel), POD 13 (middle left panel), POD 30 (middle right panel), and POD 18 (bottom panel) modes. The colored dashed vertical lines represent the value in the frequency domain that corresponds to the peaks of the PSD, where the frequencies are shown in the legend.

where σ is the distance from the center of the ellipse and its focal points. Although the forms of the dispersion relations (Equations (11) and (12)) are rather similar to the case of a waveguide with a circular cross section, the functions involved in Equations (11) and (12) are Mathieu functions, rather than Bessel functions. In the above dispersion relations, $\Xi_m^{E,O}$, $\Theta_m^{E,O}$, and $\Psi_m^{E,O}$ denote the internal solution for the body wave, the internal solution for the surface wave, and the external solution, respectively. The superscripts E and O denote the even and odd solutions, and the prime denotes the derivative of the Mathieu function with respect to the confocal elliptic variable, s .

The study by Aldhafeeri et al. (2021) revealed that the cross-sectional shape introduces significant changes in the behavior of waves, as this depends on the polarization along the major or minor axis of the ellipse. It was also found that higher-order

modes are strongly influenced by the change in the eccentricity of the waveguide.

4.3. Irregular Shape Model

In reality, the cross section of sunspots is far from being regular. The dispersion relations for regular circular and elliptical cross sections reveal that these relations are sensitive to the transversal geometry of the waveguide (Aldhafeeri et al. 2021). In order to determine the property of waves and their oscillatory patterns in waveguides with an irregular cross section, a numerical approach was used to determine the eigenfunctions and associated eigenvalues. For this problem, we used a Cartesian coordinate system, assuming the photospheric level to be the xy -plane and the vertical direction to be along the vertical z -axis. The spatial structure of the

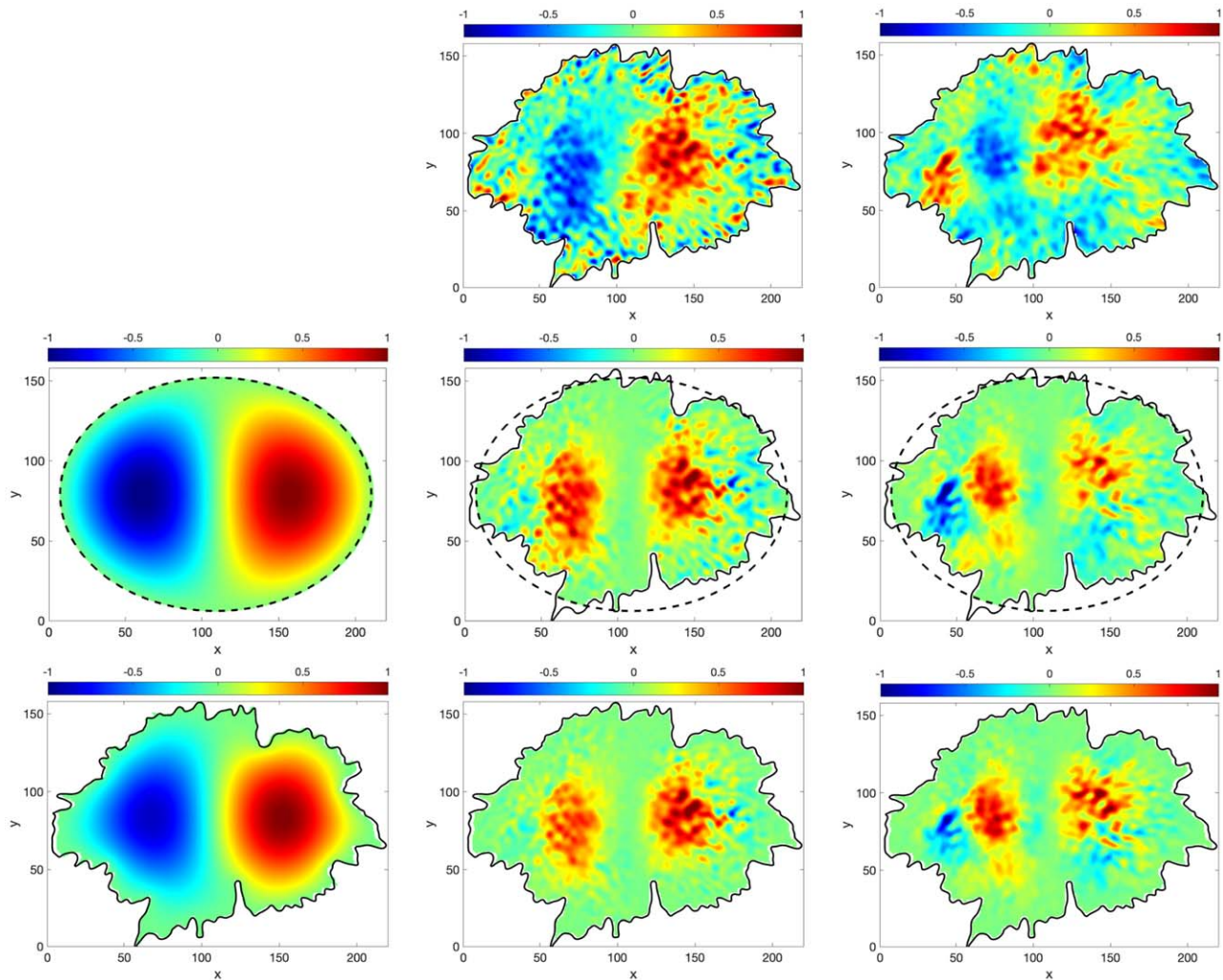


Figure 10. This figure displays the 14th POD (top row, left panel) and DMD modes (top row, right panel) with a frequency of 5.8 mHz, which has an azimuthal symmetry corresponding to the fundamental slow body kink mode. The 3D visualization of this mode is shown in Figure 22 in the Appendix.

eigenfunctions is physically constrained by the cross-sectional shape of the waveguide. The governing equation of the longitudinal velocity perturbation, v_z , was derived and solved by using the observed cross-sectional shape, where the shape is obtained by taking the threshold level of the umbra and setting $v_z = 0$ at the umbra/penumbra boundary to be consistent with the observational data.

By assuming linear MHD perturbations, the time-independent Helmholtz equation was derived for the vertical component of velocity perturbation, v_z , of the form

$$\frac{\partial^2 v_z}{\partial x^2} + \frac{\partial^2 v_z}{\partial y^2} - m_i^2 v_z = 0, \quad (14)$$

where m_i^2 is the eigenvalue defined by Equation (9). Equation (14) was solved by assuming a Dirichlet-type boundary condition, i.e., at the boundary of the magnetic waveguide, the z -component of the velocity perturbation vanishes. With this type of boundary condition, the numerical solution describes only slow body modes, which constitutes a limitation of this model. Body waves are guided waves whose longitudinal velocity amplitude is zero on the boundary of the waveguide, while taking their maximum value inside the waveguide. By choosing this type of boundary condition, we

disregard those modes (known as surface modes) whose velocity amplitude is not zero on the boundary. Of course, the POD/DMD techniques can also recover surface waves; see Section 5.1.

In order to apply the above approach to observations (line intensity), it is more convenient to write Equation (14) in terms of density perturbation, ρ . The relationship between the density and longitudinal velocity component is

$$v_z = \frac{k_z c_i^2}{\omega \rho_0} \rho, \quad (15)$$

where ρ_0 is the unperturbed density that corresponds to the equilibrium state (Aldhafeeri et al. 2021). From Equation (15), it follows that the evolution of the density perturbation is governed by a similar Helmholtz equation. In general, all of the dominant compressive variables are proportional to each other; therefore, they can be assumed to be governed by a Helmholtz-type equation.

5. MHD Wave Mode Identification and Discussion

The POD and DMD techniques were applied on the two data sets associated with the sunspots, shown in Figure 1. The

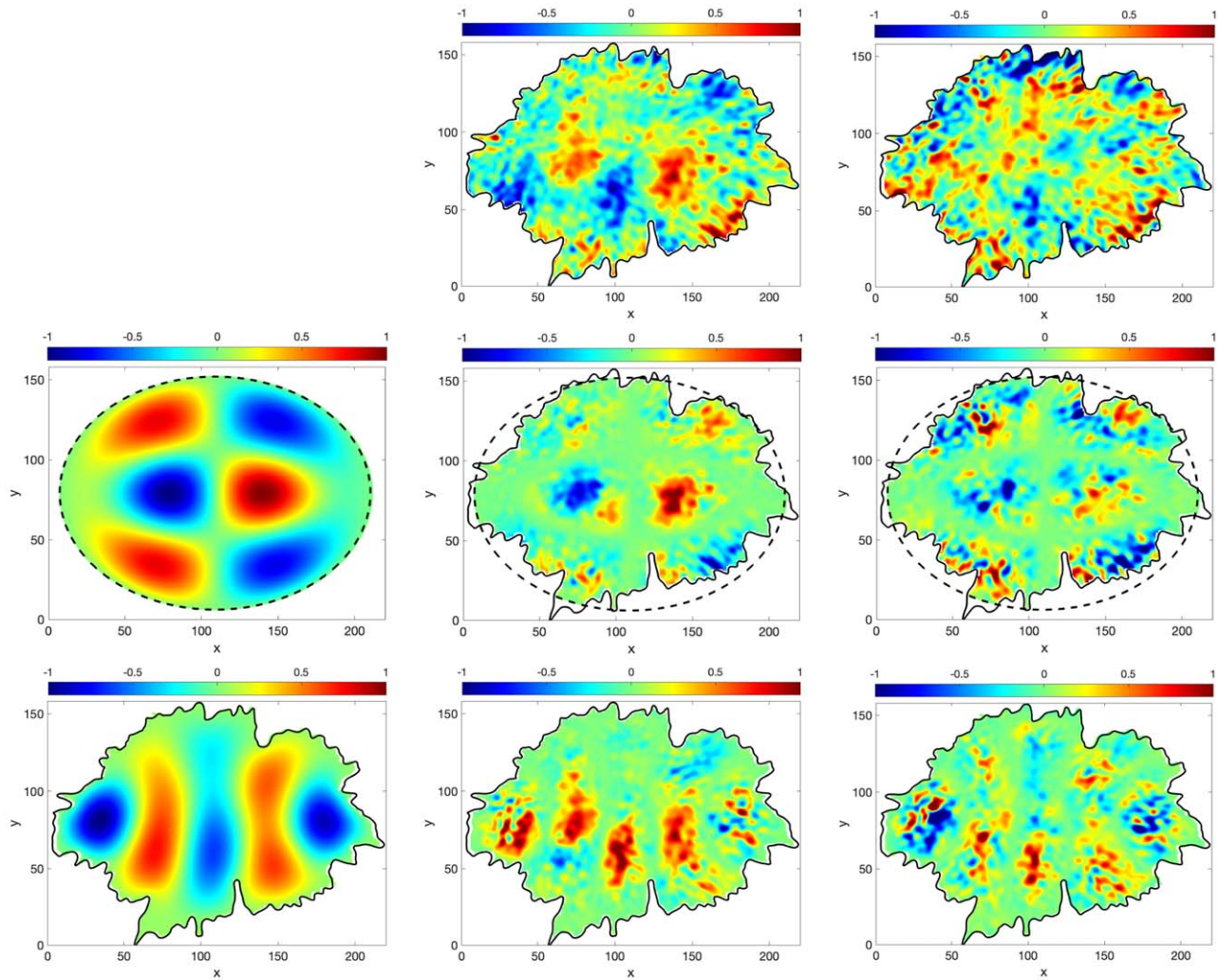


Figure 11. This figure displays the 30th POD (top row, left panel) and DMD mode (top row, right panel) with a frequency of 5.3 mHz, which has an azimuthal symmetry of the slow body kink overtone mode. The 3D visualization of this mode is shown in Figure 22 in the [Appendix](#).

oscillatory pattern of the modes recovered with the help of these techniques is compared with the results drawn from theoretical models constructed for a waveguide with cylindrical, elliptical, and irregular cross sections. The comparison is quantified by means of a cross-correlation analysis (Di Stefano et al. 2005; Tahmasebi et al. 2012) calculated on a pixel-by-pixel basis. The result of the correlation is a number between 1 and -1 , where 1 means that the two pixels have a linear correlation, while -1 denotes a linear anticorrelation.

Furthermore, as POD provides information about the temporal evolution of the coefficients of the POD modes, we can determine the power spectrum density (PSD), which will show the most dominant frequencies of the modes. Since DMD identifies modes in terms of their frequency, and by using the magnetoacoustic parameters m_i and \tilde{m}_i for the cylindrical and elliptical models, respectively, the longitudinal wavenumber, k_z , was obtained by using Equation (9) for the sunspot with a circular cross-sectional shape (see Table 1) and Equation (13) for the sunspot with an elliptical cross-sectional shape (see Table 2). Here $\omega = 2\pi f$ is the angular frequency, f refers to frequency in hertz, $c_i = 10 \text{ km s}^{-1}$ is the assumed sound speed, $v_{A_i} = 4c_i$ is the Alfvén speed, and $\sigma^2 = 0.4174$. With the help of these quantities, the wavelength ($\lambda = 2\pi/k_z$) of the waves and the phase speed ($V_{\text{ph}} = f\lambda$) were calculated for the MHD

modes identified by our analysis. The 3D visualizations of the POD and DMD modes for the circular and elliptical sunspots are provided in the [Appendix](#) (see Figures 21 and 22). The 3D surface was immersed in the volume rendering of the theoretical MHD wave model of the irregular cross-sectional shape.

Let us start with the sunspot with a circular cross-section shape shown in the upper left panel of Figure 1. The analysis was applied on the ROI represented by the blue box in the upper right panel of the same figure, where the umbra/penumbra boundary is shown by a solid black line with an intensity threshold level of 0.85. In addition to the fundamental slow body sausage mode (shown in Figure 2) and the fundamental slow body kink mode (Figure 3) identified previously (see, e.g., Albidah et al. 2021), the POD and DMD analysis reveals the existence of the higher-order MHD wave modes.

The POD mode that can be interpreted as an MHD wave mode is the 19th mode, which has the azimuthal symmetry of a slow body sausage overtone mode, i.e., a mode with more than one radial node, and the DMD mode that corresponds to the spatial structure has a frequency of 5.6 mHz, as shown in Figure 4. The PSD of the time coefficient of POD 19 has a mix

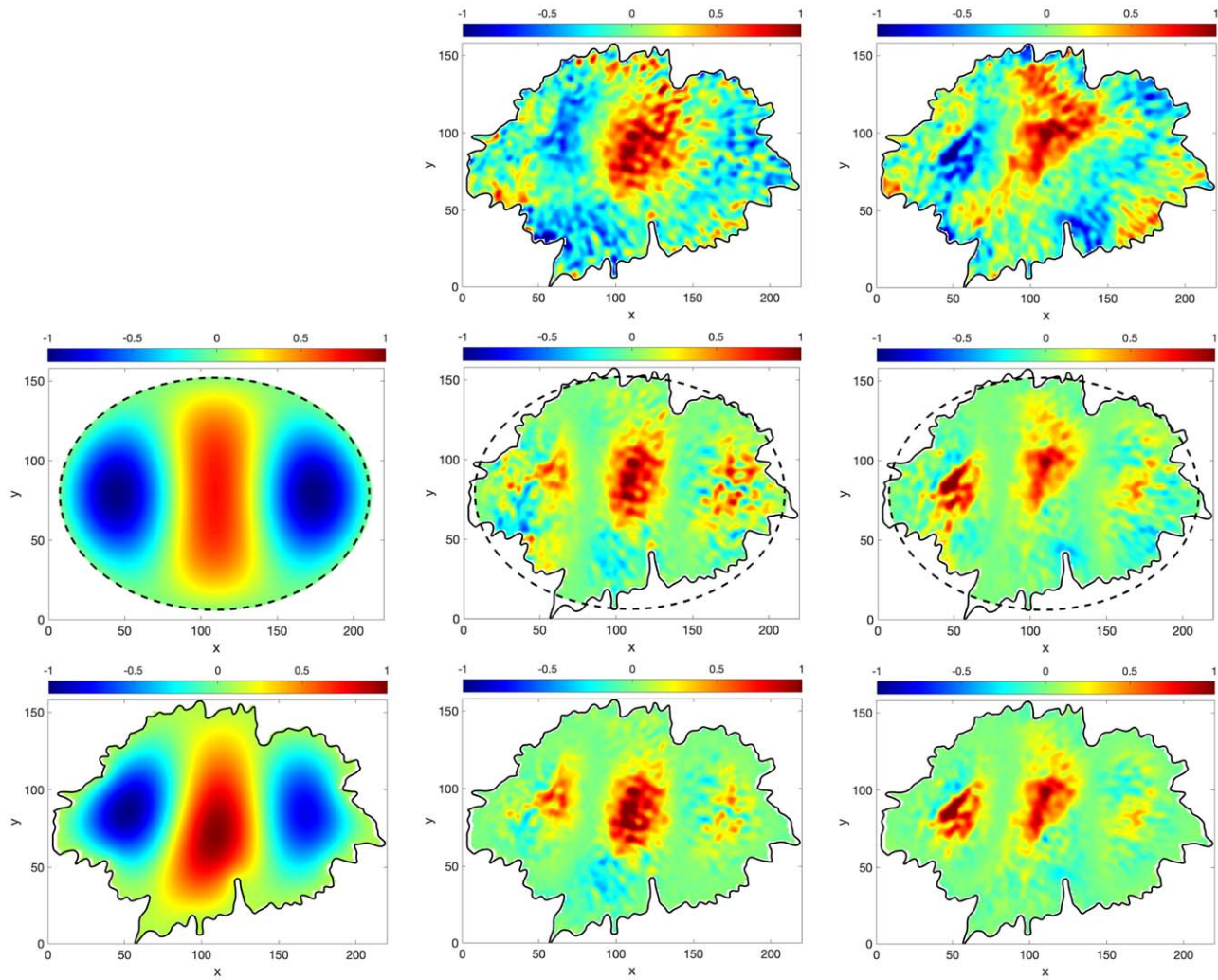


Figure 12. This figure displays the 13th POD (top row, left panel) and DMD mode (top row, right panel) with a frequency of 5.6 mHz, which has an azimuthal symmetry of the slow body fluting mode ($n = 2$). The 3D visualization of this mode is shown in Figure 22 in the [Appendix](#).

of peaks around 4.3, 5.4, and 6.5 mHz on its frequency domain, as shown in the left panel of Figure 7.

The next POD mode that can be interpreted as an MHD wave mode is the 20th component of the POD ranking, and it is visible in the DMD, too. This mode has a frequency of 7.6 mHz and an azimuthal symmetry corresponding to a slow body fluting mode ($n = 2$), as shown in Figure 5. The PSD of the 20th POD mode shows a mix of peaks around 3.7, 5.8, and 7.4 mHz, as shown in the middle panel of Figure 7. Finally, the last mode that was detected by the POD and DMD analysis that shows an azimuthal symmetry of a slow body fluting mode ($n = 3$) is the 26th POD component and the DMD mode that corresponds to 7.5 mHz, as shown in Figure 6. The PSD of the 26th POD mode shows a mix of peaks at around 3.2 and 7.2 mHz, as shown in the right panel of Figure 7.

It is expected that some of the PSDs of the POD modes may have a mix of peaks in their frequency domain, and this is one disadvantage of the POD technique, making it difficult to decide which frequency is relevant for the mode identification. However, this ambiguity is resolved by the DMD technique by taking the peaks and finding the DMD mode that corresponds to the peaks, allowing us to make a decision on which DMD mode has a spatial structure similar to the mode recovered by

means of POD; hence, we consider the distinct frequency of that DMD mode.

The sunspot with an elliptical cross-sectional shape is shown in the lower left panel of Figure 1. The POD and DMD analysis was applied to the ROI shown by the blue box in the lower right panel of the same figure, where the umbra/penumbra boundary is shown by a solid black line with an intensity threshold level at 0.4. The first POD mode that can be interpreted as an MHD wave is the first POD mode that shows the symmetry of the fundamental slow body sausage mode, and the associated DMD mode corresponds to 3.4 mHz, as shown in Figure 8. The PSD of the time coefficient of POD 1 shows peaks around 3.5 and 6.8 mHz, as shown in the top left panel of Figure 9. The next mode that can be identified in our data is the fundamental slow body kink mode, and the POD mode that shows a high correlation with this mode of oscillation is POD 14, as shown in Figure 10. The PSD of the time coefficient of POD 14 shows a clear peak at 5.88 mHz (top right panel of Figure 9). The DMD mode that shows an azimuthal symmetry with the fundamental kink is the DMD mode that corresponds to 5.8 mHz, as shown in Figure 10.

It is important to note that in the case of fundamental modes (both sausage and kink body modes), the change in the shape

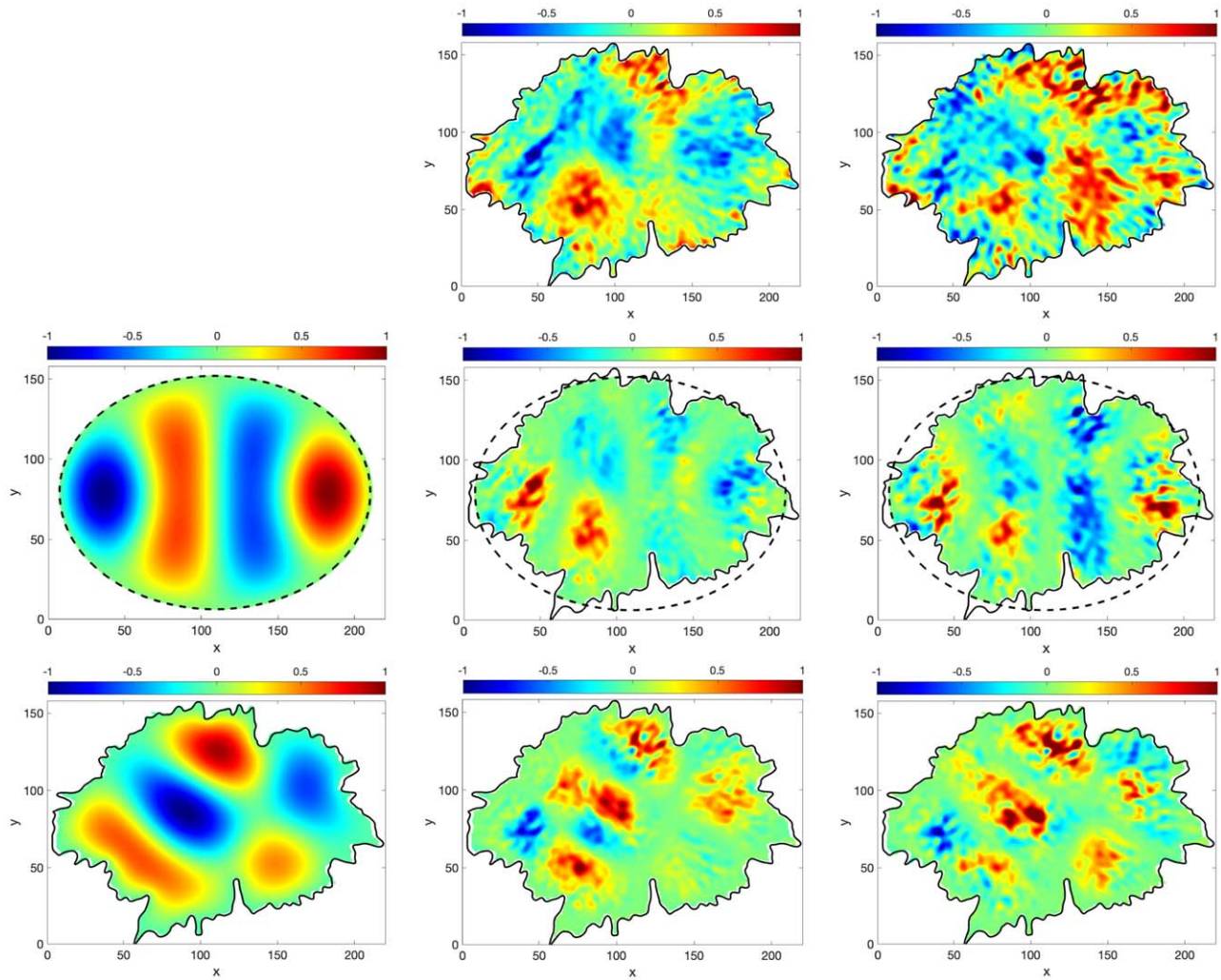


Figure 13. This figure displays the 18th POD (top row, left panel) and DMD mode (top row, right panel) with a frequency of 6.2 mHz, which has an azimuthal symmetry of the slow body fluting mode ($n = 3$). The 3D visualization of this mode is shown in Figure 22 in the [Appendix](#).

of the cross section (from cylindrical, to elliptical, and, finally, to an irregular shape) does not introduce significant changes in the morphology of waves, meaning that these modes can be confidently studied in regular shapes. The above statement proves to be incorrect for higher-order modes. The 30th POD mode and the DMD mode that corresponds to 5.3 mHz show a high correlation with the slow body kink overtone mode, as shown in Figure 11. The PSD of the time coefficients of the 30th POD shows a peak around 5.6 mHz, as displayed in the right panel of the middle row of Figure 9. The difference in the morphology of this wave between the pattern prediction of an elliptical and realistic (irregular) waveguide is remarkable, making the identification of the mode from observation misleading. Next, the 13th POD mode and the DMD mode that corresponds to 5.6 mHz are the modes that can be interpreted to have a higher correlation with the slow body fluting mode ($n = 2$), as shown in Figure 12. The PSD of POD 13 shows a peak at 5.8 mHz, visible in the left panel of the middle row of Figure 9. Finally, the last mode is the slow body fluting mode ($n = 3$), identified as the 18th POD mode and the associated DMD mode with a frequency of 6.2 mHz, as shown in Figure 13. The PSD of the POD 18 mode has a peak around 6.08 mHz, as shown in the bottom left panel of Figure 9.

Apart from the sensitivity of the modes on the cross-sectional shape of the magnetic waveguide, it is also important to note that there is a higher correlation between the observed modes and the predictions of the model corresponding to the irregular shape. We should also note that there is no complete agreement between the observed modes in either the circular or elliptical cross-section sunspot and the theoretical models, and this disagreement can be attributed to the assumptions made in the theoretical models regarding the constant values of the temperature, density, pressure, and magnetic field inside the magnetic flux tube. In reality, the magnetic flux tubes are inhomogeneous in the transversal direction (see, e.g., observations of intensity provided by high-resolution observations by, to name but a few, Gopalakrishnan et al. 2013 and Fritts et al. 2017). Furthermore, in the theory of guided MHD waves (see, e.g., Edwin & Roberts 1983), modes are monochromatic, and the lower-order MHD wave modes have a lower frequency than the higher-order modes; however, this holds true only when the wavenumber, k_z , is constant. In the family of identified modes in the present study, there are some higher-order modes having a lower frequency than the lower-order modes; however, they have different wavenumbers, as shown in Tables 1 and 2.

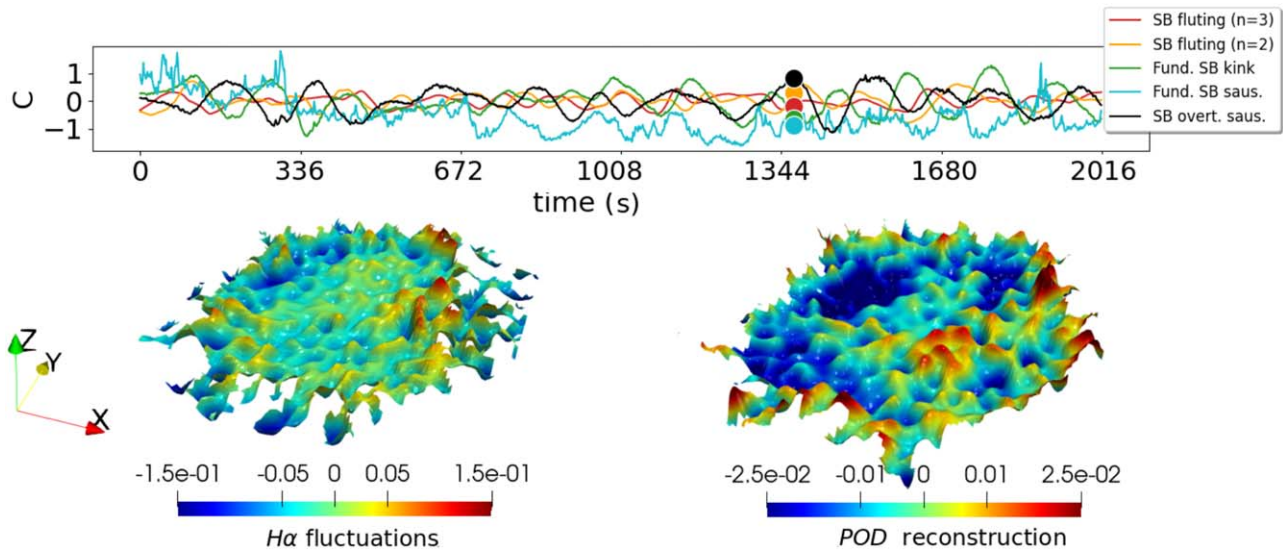


Figure 14. Intensity fluctuations in the circular sunspot. The top panel shows the time coefficient, C , for the POD modes identified as MHD waves: slow body (SB) sausage overtone, SB fundamental sausage, SB fundamental kink, SB fluting ($n = 2$), SB fluting ($n = 3$). The colors of the lines and circles depict the detected MHD wave modes, and the position of the circles indicates the time used for the plots in the bottom panels. The bottom left panel presents a 3D surface plot of the umbra where the z -direction describes the oscillations in the $H\alpha$ observations, and it is colored by the observed intensity fluctuations at time $t = 1450.7$ s. The bottom right panel is the 3D surface of the POD reconstruction of the intensity fluctuations using only the POD modes identified as MHD waves. The 3D surface is colored by the intensity fluctuations at time $t = 1450.7$ s. An animation of this 3D visualization can be found in the online Journal.

(An animation of this figure is available.)

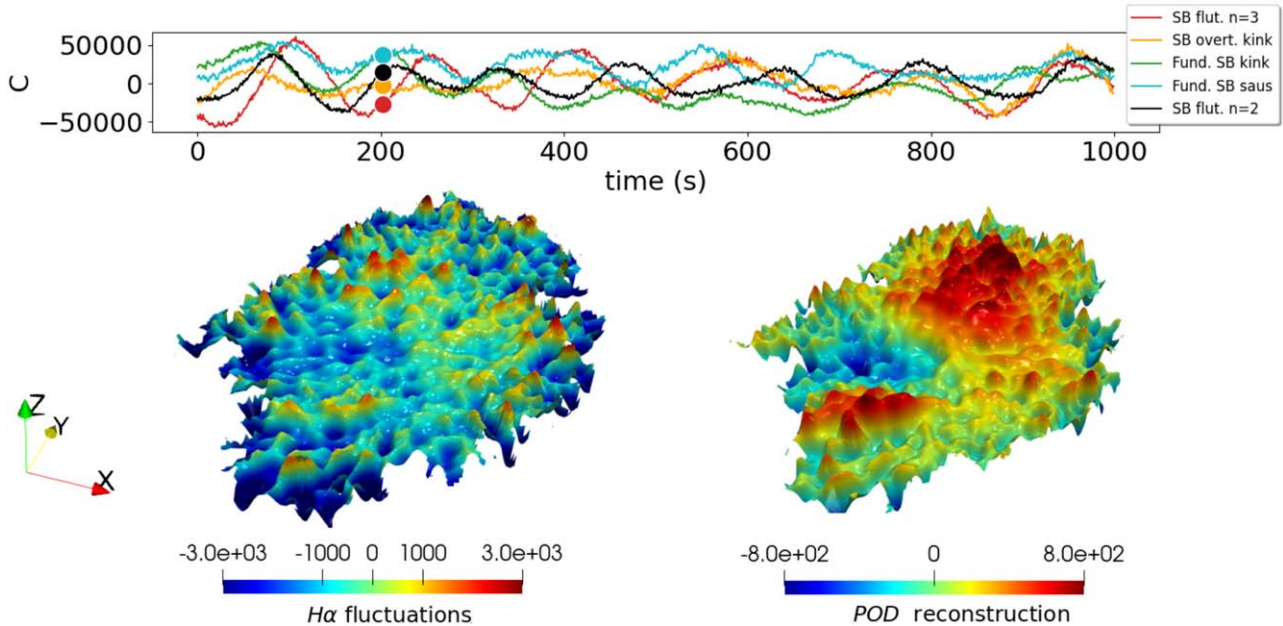


Figure 15. Intensity fluctuations in the elliptical sunspot. The top panel shows the time coefficient, C , for the POD modes identified as MHD waves: slow body (SB) fluting ($n = 2$), SB fundamental sausage, SB fundamental kink, SB overtone kink, SB fluting ($n = 3$). The colors of the lines and circles depict the detected MHD wave modes, and the position of the circle indicates the time used for the plots in the bottom panels. The bottom left panel presents a 3D surface plot of the umbra where the z -direction describes the oscillations in the $H\alpha$ observations, and it is colored by the observed intensity fluctuations at time $t = 202$ s. The bottom right panel is the 3D surface of the POD reconstruction of the intensity fluctuations using only the POD modes identified as MHD waves. The 3D surface is colored by the intensity fluctuations at time $t = 202$ s. For the POD reconstruction, we only used the POD modes identified as MHD waves. An animation of this 3D visualization can be found in the online Journal.

(An animation of this figure is available.)

One advantage of using the POD and DMD techniques for the identification of MHD modes in sunspots is the opportunity to detect a high number of MHD wave modes in one single sunspot, as these techniques provide a number of modes equal to the number of snapshots of the data set. The challenge is, however, to select and identify those modes that are physical.

Other techniques have their own limitation in identifying MHD waves in a sunspot. For example, the limitation of Fourier filtering is that it applies a wide range of bandpass filters. In the case of the circular sunspot, our earlier study (Albidah et al. 2021) identified the fundamental slow body kink mode with a frequency of 5.88 mHz and the slow body sausage overtone

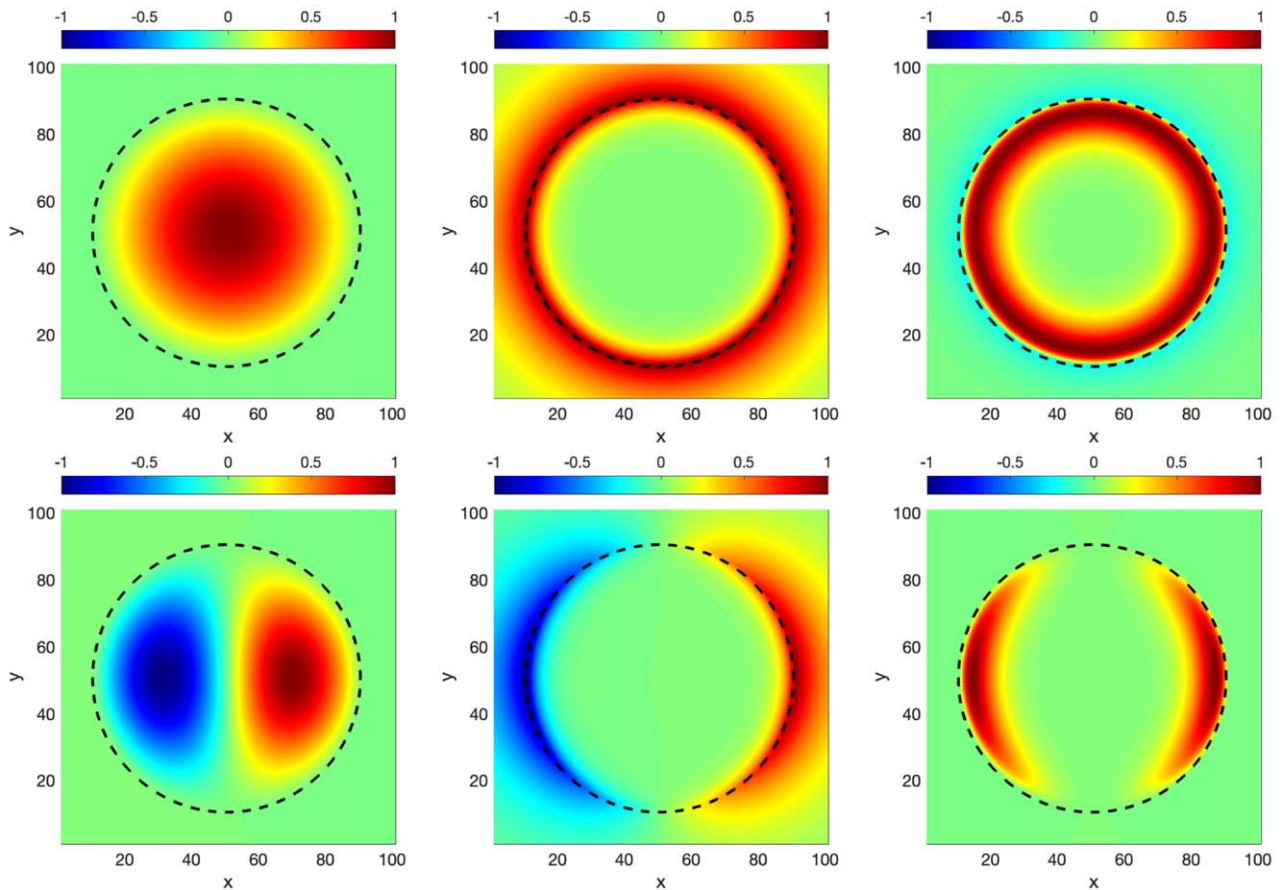


Figure 16. Sausage mode (first row) and kink mode (second row) of the cylindrical magnetic flux tube, where the first column shows the slow body mode, the second column shows the slow surface mode, and the third column shows the cross-correlation between the first and second columns.

with a frequency of 5.61 mHz. However, in the original analysis by Jess et al. (2017), using the same sunspot, they applied a $k-\omega$ Fourier filter ($0.45-0.90 \text{ arcsec}^{-1}$ and $5-6.3 \text{ mHz}$) that resulted in the identification of only the slow body kink mode. In general, higher-order modes cannot be detected, and this can be attributed to the fact that these modes have less energy than the fundamental modes, so it is expected that the spectrum is dominated by the fundamental modes. The POD and DMD techniques are able to address this shortcoming.

Figures 14 (for the circular sunspot) and 15 (for the elliptical sunspot) illustrate the ability of the POD technique to capture the portion of the umbral oscillations that are due to MHD wave modes among the observed intensity fluctuations. The top panel displays the POD time coefficient for the five detected MHD wave modes within a given time interval: 1000 s for the elliptical sunspot and 2016 s for the circular one. The lines and circles are color coded by the MHD wave mode, and the position of the circles indicates the value of time used for the plots in the bottom panels. The bottom left panels show the 3D surface representation of the original sunspot oscillations, while in the right panels, we see the reconstructed oscillations using the POD modes identified as MHD wave modes. The POD technique separates the effects of oscillations that are due to wave propagation, enhancing the expected wave pattern in the umbra. Animated movies for Figures 14 and 15 are available in the online Journal.¹⁰ The

analyzed sunspots present a considerable discrepancy for the values of the time coefficients, as the dynamics of the spatial modes changes considerably for different umbra geometry and size. Although there is a considerable difference between the POD-reconstructed oscillation intensity and the original perturbations, this discrepancy is expected, as the POD modes have less energy than the other “nonphysical” modes detected by POD. The low contribution of wave propagation to the observed oscillations may be a consequence of different issues (i.e., global modes, locally excited fluctuations) for the global variance of the oscillatory field in a sunspot. This reinforces the POD as a valuable tool to apply to wave detection in sunspots, as other methodologies require properly filtering the data in order to disentangle and detect the resonant modes.

5.1. Surface Wave Identification

The POD and DMD techniques can also be applied to identify surface modes. In the POD analysis performed on the circular sunspot, it was found that there were two modes that have the characteristics of surface waves: the POD 10 mode (see the middle panel of Figure 18), which shows the azimuthal symmetry corresponding to the fundamental (slow or fast) surface sausage mode, and the POD 6 mode (see the middle panel of Figure 19), which has a pattern close to the fundamental (slow or fast) surface kink mode. Our theoretical model is restricted to the identification of slow body modes, i.e., modes corresponding to $v_z=0$ at the umbra/penumbra boundary (see Section 4.3). Therefore, in the framework of this

¹⁰ Copies of the animations are also available on the University of Sheffield Plasma Dynamics Group’s visualizations Google Sites webpage: <https://sites.google.com/sheffield.ac.uk/pgd/visualisations>.

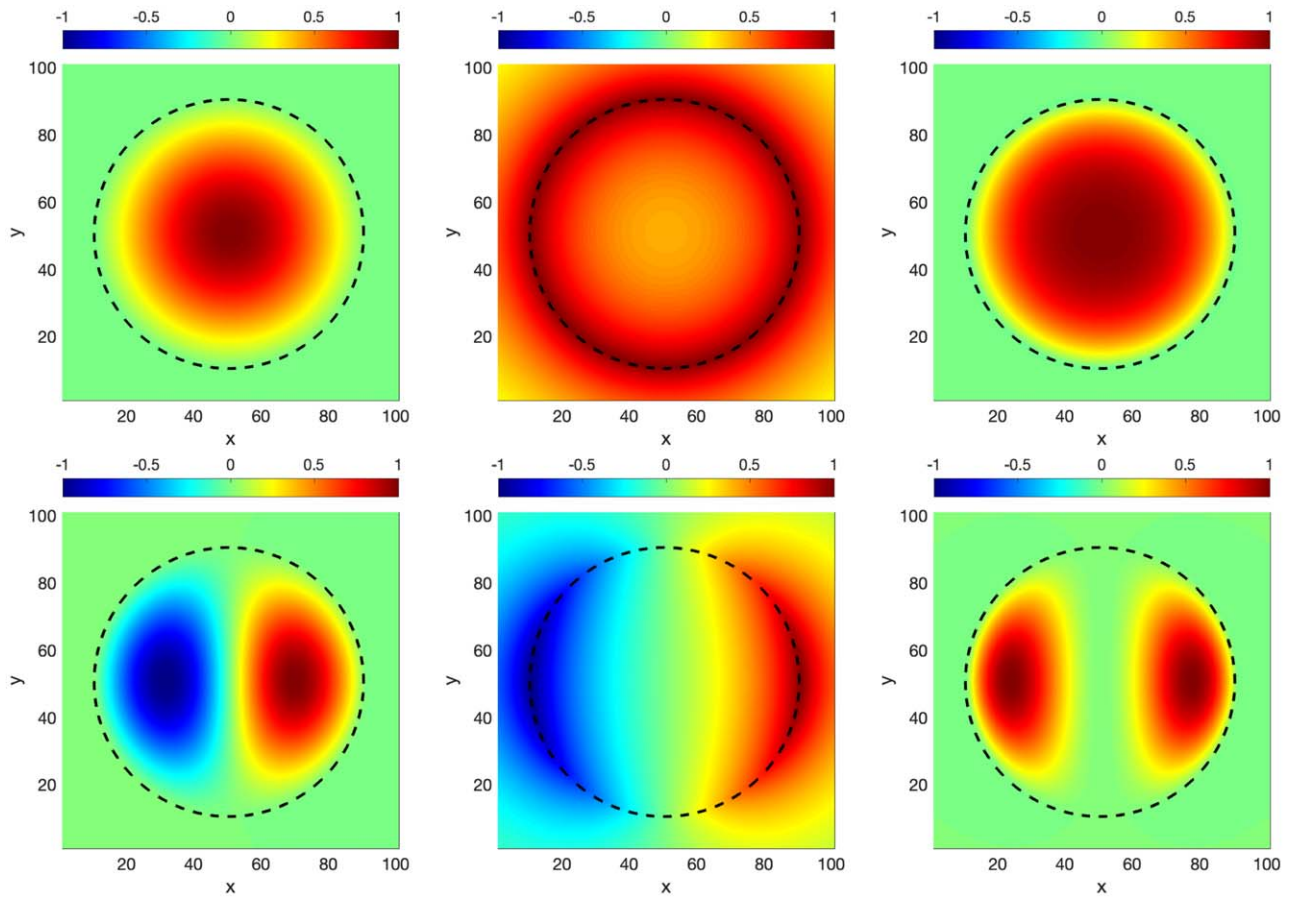


Figure 17. Sausage mode (first row) and kink mode (second row) of the cylindrical magnetic flux tube, where the first column shows the slow body mode, the second column shows the fast surface mode, and the third column shows the cross-correlation between the first and second columns.

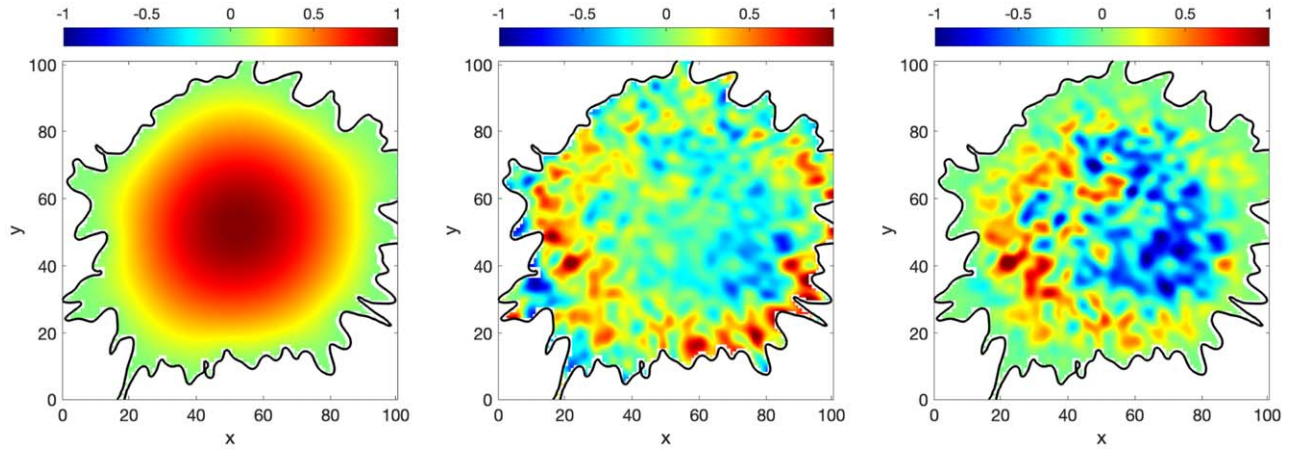


Figure 18. Fundamental slow body sausage mode as shown in Figure 2 (left panel), the spatial structure of POD 10 (middle panel), and the cross-correlation between the left and middle panels (right panel).

study, cross-correlation with possible surface modes detected with POD/DMD and their direct theoretical counterparts cannot be performed. Nevertheless, the cross-correlation between the theoretical slow body and slow surface modes in a magnetic cylinder produces a distinctive closed ring for the sausage mode and a broken ring for the kink mode (see Figure 16) with a clear in-phase relationship. Moreover, the cross-correlation between the slow body mode and the fast surface mode also provides an in phase, but the spatial structure

is very close to the slow body eigenmode shown in Figure 17. These distinctive signatures at least provide an indirect way of detecting slow and fast surface modes in the observational data.

The POD modes that appear most likely to be surface modes have been correlated with the fundamental slow body sausage and kink modes as shown in Figures 18 and 19, respectively. In Figure 18 (middle panel), the red ring is present, indicating a slow surface sausage mode, but the blue regions of antiphase inside the red ring and on the outer left edge cannot be

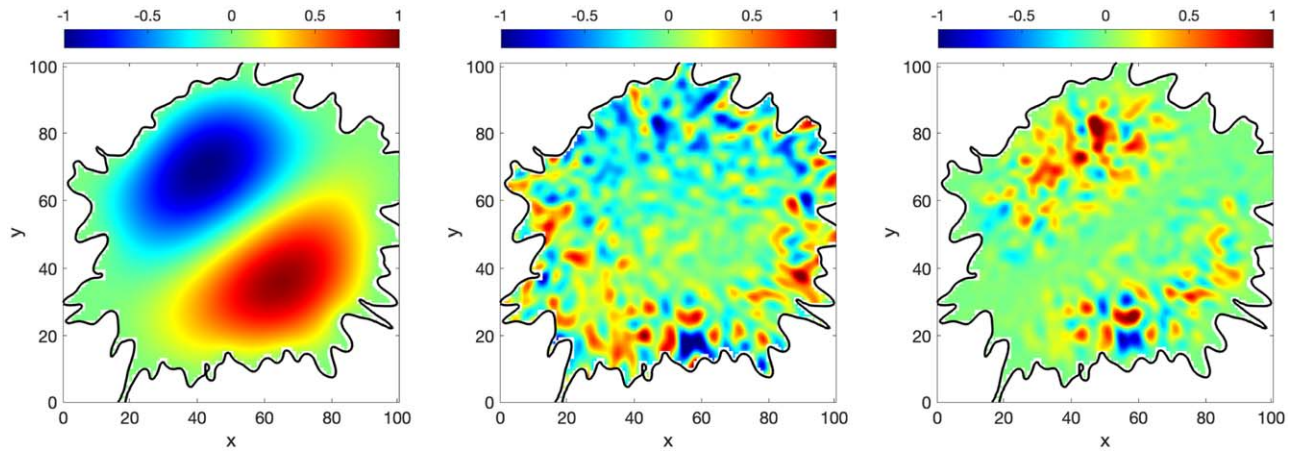


Figure 19. Fundamental slow body kink mode as shown in Figure 3 (left panel), the spatial structure of POD 6 (middle panel), and the cross-correlation between the left and middle panels (right panel).

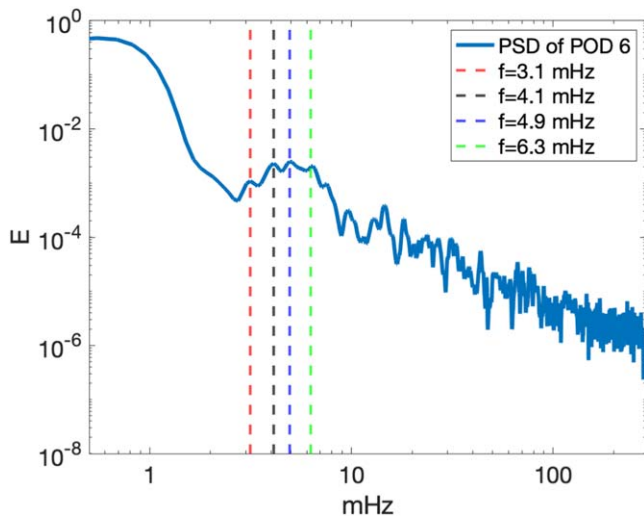


Figure 20. The PSD of the time coefficients of the POD 6 mode.

explained by the theoretical model. The antiphase regions are even more prominent in Figure 18 (right panel) and are also not predicted for the theoretical fast surface mode. The cross-correlation for the POD 6 mode shows stronger agreement with a fast surface kink mode as shown in Figure 19, although there are still some small antiphase regions that are not consistent with the theoretical model. Figure 20 shows the PSD of the time coefficient of POD 6, which shows a mix of peaks.

6. Summary and Conclusions

The present study provides clear evidence of MHD sausage ($n=0$) and kink mode ($n=1$) overtones and higher-order ($n \geq 2$) fluting modes in sunspots. The results obtained are a significant extension of the previous studies by Jess et al. (2017) and Albidah et al. (2021), where MHD modes were recovered for the case of an approximately circular sunspot. First, the mode detection was carried out by means of the POD and DMD techniques. Our results were compared with their theoretical counterparts obtained assuming a cylindrical magnetic flux tube, as well as with

the model of a magnetic flux that corresponds to the actual irregular shape of the umbra boundary.

Second, the same techniques were also applied to a sunspot whose shape is close to an elliptical cross section and compared the obtained results with the theoretical predictions of waves in an elliptical waveguide, as well as an irregularly shaped magnetic flux tube corresponding to the actual shape of the umbra boundary. The comparison between modes detected in observational data and in theoretical models was carried out by means of cross-correlation analysis calculated on a pixel-by-pixel basis. The correlation results demonstrate that the higher-order MHD modes are more strongly affected by irregularities in the sunspot shape.

The vertical wavenumber, k_z , and mode frequencies have been calculated by using the magnetoacoustic wave parameter (m_i) and Equation (9) for sunspots with a circular cross-sectional shape and Equation (13) for sunspots with an elliptical cross-sectional shape (see Tables 1 and 2).

The existence of these MHD waves was theoretically predicted almost 40 yr ago (see, e.g., Edwin & Roberts 1983), so our study offers what is probably one of the first pieces of observational evidence for the existence of higher-order modes in the chromosphere. Only a few papers reported their observational presence (see, e.g., Yuan 2015; Kang et al. 2019; Stangalini et al. 2022). These waves offer an unprecedented diagnostic tool for describing the dynamical state of the plasma and the structure of the magnetic field, since they are carrying information about the medium in which they are propagating, and seismological techniques can be applied to compare observationally determined quantities with theoretical predictions to infer values that cannot be (directly or indirectly) measured. Seismology using a single wave is a sort of underdetermined system because many variables are implicit, and the variables that can be extracted are not independent (similar to a system of equations having $n \geq 2$ variables, but only $n - 1$ equations are given). The observation of at least two or more modes in the same structure helps resolve this degeneracy.

Concurrent observations of different kinds of waves (including the higher-order modes presented in our study) could allow us to more fully understand the true nature of the dynamics and comprehensively describe the plasma state and structure of the magnetic field. Potentially, our results could

help us better understand the nature and properties of modes in more realistically structured waveguides, where the sound and Alfvén speeds are spatially varying, which would modify the eigenvalues and eigenfunctions, especially of the higher-order modes.

Higher-order modes also give a more complete description of subsurface drivers. It is clear that in the present situation, we are dealing with a broadband driver. However, slow body modes are weakly dispersive, and their phase speeds are confined to a narrow band between the tube speed and internal sound speed. This means that the helioseismological approach of exploiting detected p -modes, where modes in $\omega - k$ space correspond to distinct clear ridges, would certainly be a challenge.

In addition, due to the presence of the higher-order modes (as these are the most sensitive to the shape of the waveguide), we demonstrated that using the exact cross-sectional shape of the waveguide is essential for the correct interpretation of waves.

The current study and techniques used for wave detection have important implications for the interpretation of

observational data from next-generation ground-based observing facilities (in particular, the new 4 m DKIST solar telescope).

A.B.A. acknowledges support by Majmaah University (Saudi Arabia) to carry out his PhD studies. V.F., G.V., and I.B. are grateful to the Royal Society, International Exchanges Scheme, collaboration with Chile (IES/R1/170301). V.F. and S.S.A.S. are grateful to Science and Technology Facilities Council (STFC) grant ST/V000977/1. This research has also received financial support from the European Union's Horizon 2020 research and innovation program under grant agreement No. 824135 (SOLARNET). A.A. acknowledges the Deanship of Scientific Research (DSR), King Faisal University, Al-Hassa (KSA), for financial support.

Appendix

The 3D visualizations of the observed modes, as well as a volume rendering of the theoretical MHD wave model, are shown in Figures 21 and 22 for the circular and the elliptical sunspot, respectively.

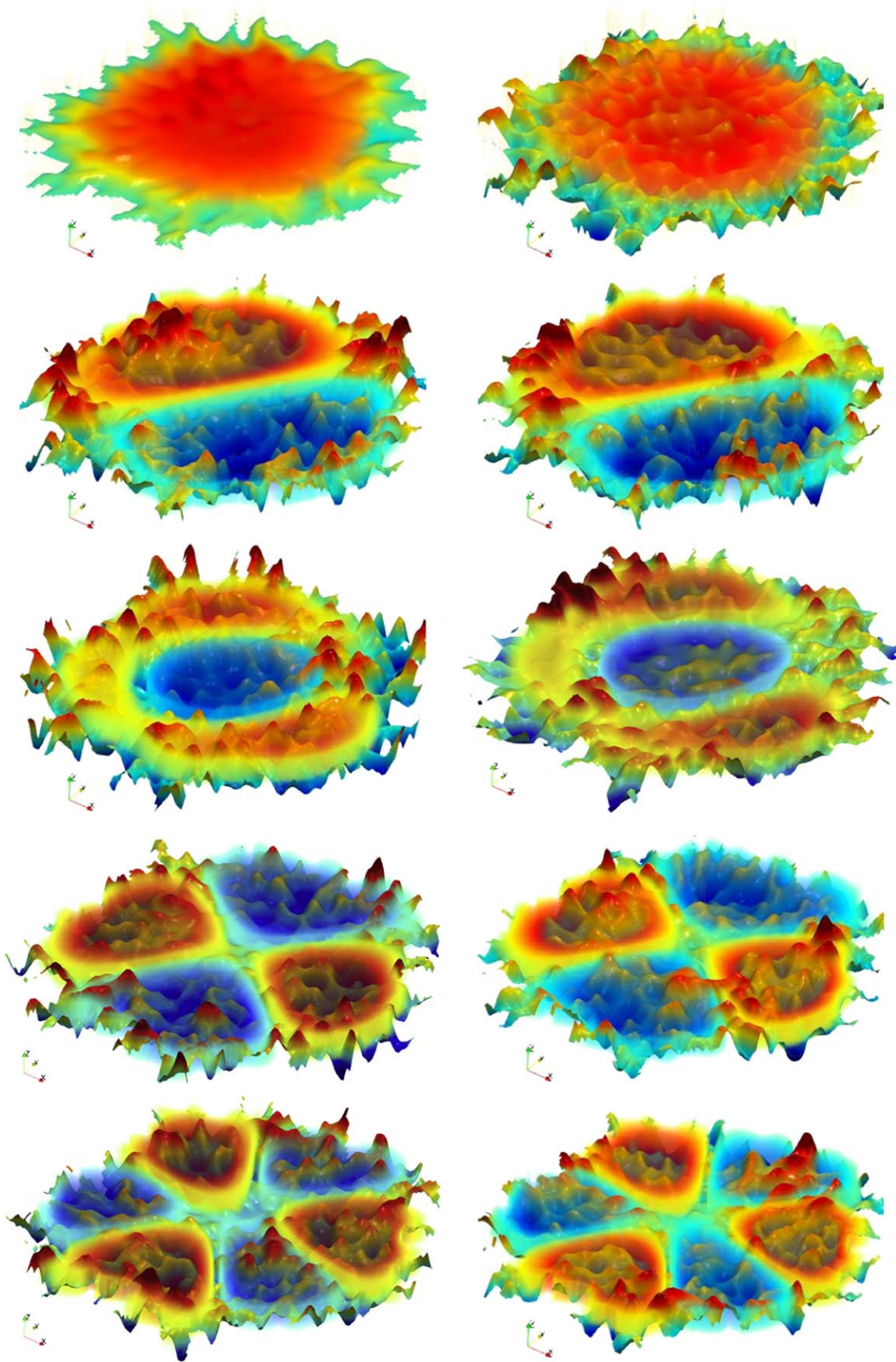


Figure 21. The 3D surface plot of the POD (first column) and DMD (second column) modes obtained for the case of a circular sunspot, as well as a volume rendering of the theoretical MHD wave model, which uses the same color code as the POD and DMD modes. Rows refer to particular identified MHD modes, that is, the fundamental slow body sausage mode (first row), fundamental slow body kink mode (second row), slow body sausage overtone (third row), $n = 2$ slow body fluting mode (fourth row), and $n = 3$ slow body fluting mode (fifth row).

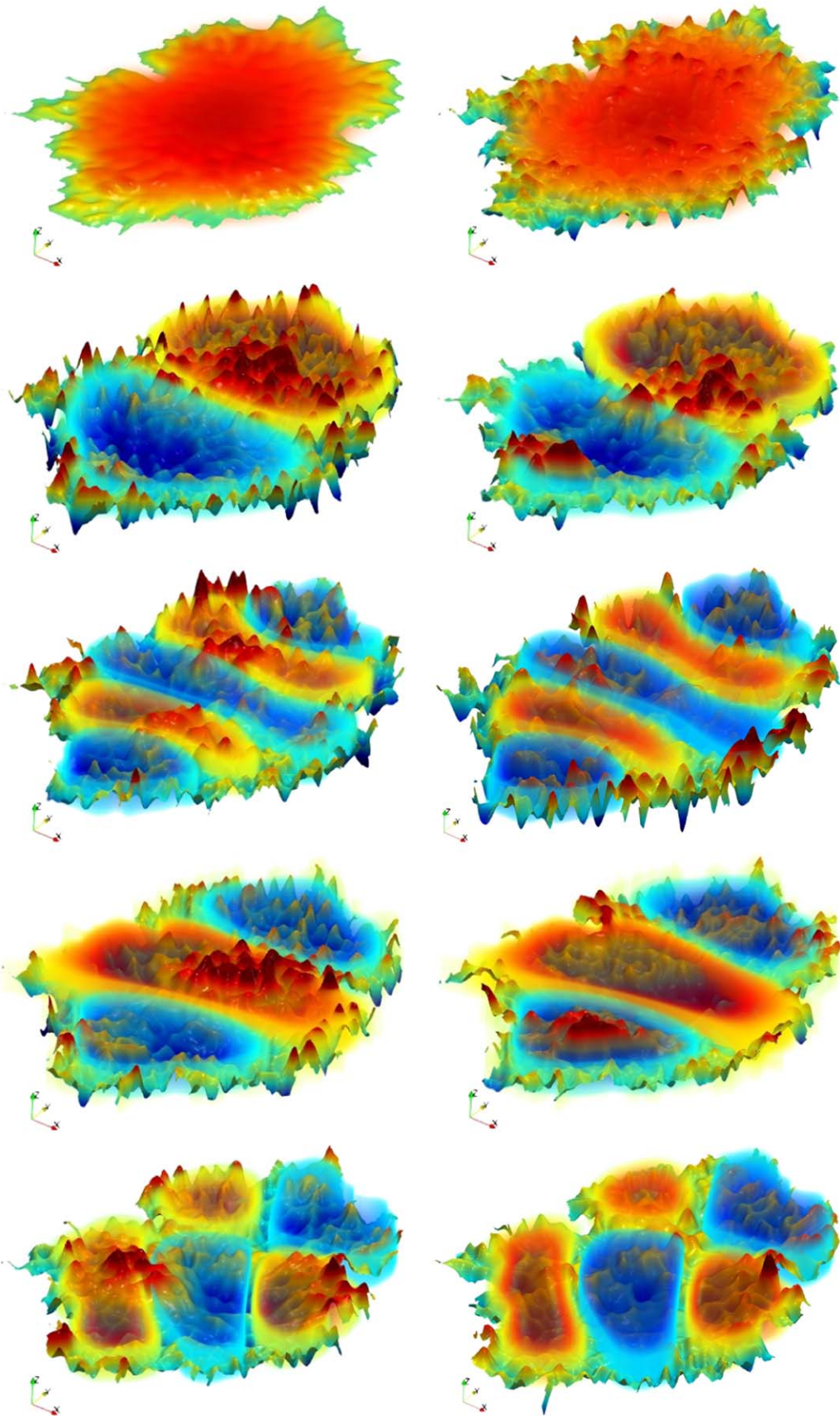












Figure 22. The visualization techniques are the same as in Figure 21, but here the rows refer to the MHD wave mode recovered in the elliptical sunspot, that is, the fundamental slow body sausage mode (first row), fundamental slow body kink mode (second row), slow body overtone kink mode (third row), $n = 2$ slow body fluting mode (fourth row), and $n = 3$ slow body fluting mode (fifth row).

ORCID iDs

A. B. Albidah  <https://orcid.org/0000-0001-7314-1347>
 V. Fedun  <https://orcid.org/0000-0002-0893-7346>
 A. A. Aldhafeeri  <https://orcid.org/0000-0003-2220-5042>
 I. Ballai  <https://orcid.org/0000-0002-3066-7653>
 W. Brevis  <https://orcid.org/0000-0001-8161-4677>
 D. B. Jess  <https://orcid.org/0000-0002-9155-8039>
 J. Higham  <https://orcid.org/0000-0001-7577-0913>
 M. Stangalini  <https://orcid.org/0000-0002-5365-7546>
 S. S. A. Silva  <https://orcid.org/0000-0001-5414-0197>
 G. Verth  <https://orcid.org/0000-0002-9546-2368>

References

- Albidah, A. B., Brevis, W., Fedun, V., et al. 2021, *RSPTA*, **379**, 20200181
 Aldhafeeri, A. A., Verth, G., Brevis, W., et al. 2021, *ApJ*, **912**, 50
 Beckers, J., & Schultz, R. 1972, *SoPh*, **27**, 61
 Beckers, J. M., & Tallant, P. E. 1969, *SoPh*, **7**, 351
 Berry, M., Magstadt, A., & Glauser, M. N. 2017, *PhFI*, **29**, 020706
 Christopoulou, E., Skodras, A., Georgakilas, A., & Koutchmy, S. 2003, *ApJ*, **591**, 416
 Di Stefano, L., Mattoccia, S., & Tombari, F. 2005, *PaReL*, **26**, 2129
 Edwin, P., & Roberts, B. 1983, *SoPh*, **88**, 179
 Fritts, D. C., Wang, L., Baumgarten, G., et al. 2017, *JASTP*, **162**, 57
 Gopalakrishnan, S. G., Marks, F., Jr., Zhang, J. A., et al. 2013, *J. Atmos. Sci.*, **70**, 524
 Grant, S. D. T., Jess, D. B., Zaqarashvili, T. V., et al. 2018, *NatPh*, **14**, 480
 Higham, J., & Brevis, W. 2018, *Exp. Therm. Fluid Sci.*, **90**, 212
 Higham, J., Brevis, W., & Keylock, C. 2018, *J. Hydraul. Res.*, **56**, 796
 Higham, J., Brevis, W., Keylock, C., & Safarzadeh, A. 2017, *AdWR*, **107**, 451
 Higham, J., Shahnam, M., & Vaidheeswaran, A. 2020, *Granul. Matter*, **22**, 1
 Higham, J., Vaidheeswaran, A., Brevis, W., Nicolleau, F., & Marlow, J. 2021, *PhFI*, **33**, 045117
 Jess, D. B., De Moortel, I., Mathioudakis, M., et al. 2012, *ApJ*, **757**, 160
 Jess, D. B., Mathioudakis, M., Christian, D. J., et al. 2010, *SoPh*, **261**, 363
 Jess, D. B., Morton, R. J., Verth, G., et al. 2015, *SSRv*, **190**, 103
 Jess, D. B., Reznikova, V. E., Van Doorselaere, T., Keys, P. H., & Mackay, D. H. 2013, *ApJ*, **779**, 168
 Jess, D. B., Shelyag, S., Mathioudakis, M., et al. 2012, *ApJ*, **746**, 183
 Jess, D. B., Reznikova, V. E., Ryans, R. S. I., et al. 2016, *NatPh*, **12**, 179
 Jess, D. B., Van Doorselaere, T., Verth, G., et al. 2017, *ApJ*, **842**, 59
 Kang, J., Chae, J., Nakariakov, V. M., et al. 2019, *ApJL*, **877**, L9
 Keys, P. H., Morton, R. J., Jess, D. B., et al. 2018, *ApJ*, **857**, 28
 Khomenko, E., & Collados, M. 2015, *LRSP*, **12**, 6
 Krishna Prasad, S., Jess, D. B., & Khomenko, E. 2015, *ApJL*, **812**, L15
 Murray, N. E., & Ukeiley, L. S. 2007, *ExFI*, **42**, 79
 Nagashima, K., Sekii, T., Kosovichev, A. G., et al. 2007, *PASJ*, **59**, S631
 O'shea, E., Muglach, K., & Fleck, B. 2002, *A&A*, **387**, 642
 Pearson, K. 1901, *Lond. Edinb. Dublin Philos. Mag. J. Sci.*, **2**, 559
 Rimmele, T. R. 2004, *Proc. SPIE*, **5490**, 34
 Schmid, P. J. 2010, *JFM*, **656**, 5
 Stangalini, M., Del Moro, D., Berrilli, F., & Jefferies, S. 2011, *A&A*, **534**, A65
 Stangalini, M., Jess, D., Verth, G., et al. 2021, *A&A*, **649**, A169
 Stangalini, M., Verth, G., & Fedun, V. 2022, *NatCo*, **13**, 479
 Sych, R., Zaqarashvili, T., Nakariakov, V., et al. 2012, *A&A*, **539**, A23
 Tahmasebi, P., Hezarkhani, A., & Sahimi, M. 2012, *Comput. Geosci.*, **16**, 779
 Tu, J. H., Rowley, C. W., Luchtenburg, D. M., Brunton, S. L., & Kutz, J. N. 2014, *J. Comput. Dyn.*, **1**, 391
 Wöger, F., von der Lühe, O., & Reardon, K. 2008, *A&A*, **488**, 375
 Yuan, D. 2015, *RAA*, **15**, 1449
 Zhou, X., & Liang, H. 2017, *Ap&SS*, **362**, 46